



140  
332  
THS

This is to certify that the  
dissertation entitled

Measurement of the Diphoton Differential Cross-Section in  
pp-bar Collisions at sqrt s = 1.96 TeV

presented by

Joshua Marc Dyer

has been accepted towards fulfillment  
of the requirements for the

Ph.D. degree in Physics



*Bernard G Pope*

Major Professor's Signature

6-8-2007

Date

**PLACE IN RETURN BOX** to remove this checkout from your record.  
**TO AVOID FINES** return on or before date due.  
**MAY BE RECALLED** with earlier due date if requested.

DATE DUE	DATE DUE	DATE DUE

MEASUREMENT OF THE DIPHOTON DIFFERENTIAL  
CROSS-SECTION IN  $p\bar{p}$  COLLISIONS AT  $\sqrt{s} = 1.96$  TeV

By

Joshua Marc Dyer

A DISSERTATION

Submitted to  
Michigan State University  
in partial fulfillment of the requirements  
for the degree of

DOCTOR OF PHILOSOPHY

Department of Physics and Astronomy

2007

# ABSTRACT

MEASUREMENT OF THE DIPHOTON DIFFERENTIAL CROSS-SECTION IN

$p\bar{p}$  COLLISIONS AT  $\sqrt{s} = 1.96$  TeV

By

Joshua Marc Dyer

The diphoton differential cross-section as a function of mass up to  $300 \text{ GeV}/c^2$ ,  $q_T$  up to  $100 \text{ GeV}/c$ , and opening angle over a range of 0 to  $\pi$  radians is measured. The measurement is performed using  $1046.19 \text{ pb}^{-1}$  of data collected at Fermi National Accelerator Laboratory using the D0 detector. This analysis considers all direct diphoton states but attempts to suppress contributions due to fragmentation.

Copyright © by

Joshua Marc Dyer

2007

To my family

## ACKNOWLEDGMENTS

Many people have my gratitude in supporting me throughout my graduate education. First I need to thank my family and friends. To my bride, Kimberly, for her enduring love, attention, and strength; I could not have done it without you. To my parents for their encouragement and love. To Kimberly's parents for their assistance and enjoyment of MSU sports. To my brothers for their humor and support. To Richard, Aaron B., and Todd for their friendship after undergrad and providing plenty of comedy.

Thanks to the GEU for providing me with a community to which I could contribute and better many students' lives with what little free time I had, as well as for introducing me to Kimberly. To the Drew students for giving me an avenue to nurture my love of teaching and for helping me to see the world through others' life experiences.

Thanks to my friends at MSU including Russ, Nate, Heather, Andrew, Steve, and Gene...for all of the study sessions, games, and much needed breaks from physics. Thanks to the MSU group at Fermilab: Josh K., Adam, Joe, Rahmi, Joel, Reiner and Reinhard for orienting me to Level 2, the D0 packages, and every other bit of service work involved at the lab as well as Friday tradition and softball. Go D0nuts!

Special thanks to Jodi Wittlin and Suyong Choi for taking me under their wing and being my surrogate post-docs. They encouraged my progress in research, helped me contribute to the Higgs group, and assisted me in growing as a scientist. They were always there for me when I had questions, hit a wall, or had C++ problems...and Jodi arranged lunches at East China Inn. Also to Alex Melnitchouk and Oleksiy Atramentov for always helping whenever I had questions about photons.

To the office staff at MSU for making everything run so smoothly behind the scenes; thanks Brenda and Debbie. Thanks also to the other grads in the office Aous, Mohammed, Brian, Barath, Stefano, and Chen for helping with random questions as they occurred.

Thanks to the theory guys that provided comparison predictions. To C-P Yuan for RESBOS and some theory discussions, Jean-Philippe Guillet for running the DIPHOX code and providing the result for me, and Carl Schmidt for providing the gluon-gluon box contribution for addition to DIPHOX.

Finally, to my advisor, Bernard Pope, for his wisdom, guidance, and support. Thank you for helping me to navigate Fermilab, high energy, and finding my place in the physics community.

# TABLE OF CONTENTS

<b>LIST OF TABLES</b>	<b>ix</b>
<b>LIST OF FIGURES</b>	<b>x</b>
<b>1 Introduction</b>	<b>1</b>
<b>2 Theory</b>	<b>3</b>
2.1 The Standard Model . . . . .	3
2.2 QCD and Higgs Searches . . . . .	6
2.2.1 QCD and the Requirement of Color . . . . .	6
2.2.2 The Higgs Boson . . . . .	7
2.3 Direct Diphotons . . . . .	7
<b>3 Fermi National Accelerator Laboratory and the D0 Experiment</b>	<b>11</b>
3.1 Fermilab . . . . .	11
3.2 Accelerator and Antiproton ( $\bar{p}$ ) Production . . . . .	12
3.3 The D0 Detector . . . . .	15
3.4 Coordinate System and Variables . . . . .	15
3.5 Tracking System . . . . .	18
3.5.1 Silicon Microstrip Tracker . . . . .	18
3.5.2 The Central Fiber Tracker . . . . .	21
3.6 Preshower . . . . .	22
3.7 Calorimeter . . . . .	24
3.8 Muon System . . . . .	30
3.9 Luminosity Monitor (LM) . . . . .	30
3.10 Trigger System and DAQ . . . . .	31
3.10.1 Level 1 Trigger . . . . .	33
3.10.2 Level 2 Trigger . . . . .	33
3.10.3 Level 3 Trigger . . . . .	34
3.10.4 Data Acquisition (DAQ) . . . . .	34
3.11 D0RECO and CAF . . . . .	36

<b>4</b>	<b>Dataset and Monte Carlo</b>	<b>37</b>
4.1	Trigger . . . . .	37
4.2	Trigger Efficiencies . . . . .	40
4.3	Dataset . . . . .	43
4.3.1	Data Quality . . . . .	44
4.4	Monte Carlo . . . . .	46
<b>5</b>	<b>Photon ID and Background Study</b>	<b>47</b>
5.1	Reconstruction Algorithms . . . . .	47
5.2	Particle Signatures . . . . .	48
5.2.1	Photons . . . . .	48
5.2.2	Electrons . . . . .	48
5.2.3	Jets . . . . .	49
5.2.4	Muons . . . . .	49
5.3	Signal Variables . . . . .	49
5.4	Background . . . . .	51
5.5	Analysis Cuts and Efficiencies . . . . .	53
5.5.1	Analysis Cuts . . . . .	53
5.5.2	Cut Efficiencies . . . . .	56
<b>6</b>	<b>Cross-Section Analysis</b>	<b>63</b>
6.1	Matrix Inversion Method . . . . .	63
6.2	Efficiency Data Samples . . . . .	64
6.3	Discrimination Variables . . . . .	66
6.3.1	Phi Width . . . . .	66
6.3.2	CPS_RMS . . . . .	66
6.3.3	CPS_RMS Squared . . . . .	69
6.4	Result of Matrix Inversion . . . . .	69
6.5	Cross-Section . . . . .	75
<b>7</b>	<b>Conclusions</b>	<b>81</b>
	<b>BIBLIOGRAPHY</b>	<b>83</b>

# LIST OF TABLES

2.1	Standard Model Quarks [2]. . . . .	3
2.2	Standard Model Leptons [2]. . . . .	4
2.3	Standard Model Gauge Bosons [2, 3]. . . . .	5
3.1	Depths of the calorimeter layers. . . . .	28
4.1	Triggers by trigger list. . . . .	38
4.2	Summary of trigger efficiencies. . . . .	42
4.3	Total integrated luminosity by trigger list. . . . .	43

# LIST OF FIGURES

Images in this dissertation are presented in color.

2.1	Branching ratios of the dominant decay modes of the Standard Model Higgs boson. . . . .	8
2.2	Leading order (LO) Feynman diagrams for direct diphoton production in QED, QCD, and mixed. . . . .	9
2.3	Radiative corrections to the LO Feynman diagrams. . . . .	10
3.1	Layout of Fermilab's accelerators [9]. . . . .	14
3.2	The D0 Detector [11]. . . . .	16
3.3	Cross-section of the D0 tracking system [11]. . . . .	19
3.4	Barrel/Disk design of the SMT [11]. . . . .	19
3.5	Cross sectional view of the SMT [11]. . . . .	20
3.6	Positioning of two fiber ribbons to form a doublet [11]. . . . .	21
3.7	Cross sectional view of the CFT and associated waveguides [11]. . . . .	23
3.8	Schematics of the CPS and FPS detectors. The top right shows the CPS geometry, and the bottom right shows the FPS geometry [11]. . . . .	25
3.9	D0 calorimeter [11]. . . . .	27
3.10	Calorimeter unit cell [17]. . . . .	28
3.11	Pseudo-projective geometry and segmentation pattern of the calorimeter. . . . .	29
3.12	Designed D0 trigger scheme[17]. . . . .	32
3.13	L1 and L2 trigger flow [17]. . . . .	35
4.1	Trigger turn-on curves for OR'd single EM triggers [23]. . . . .	41
4.2	Eta vs. Phi lego plot illustrating hot cells. . . . .	45

5.1	Distributions of signal variables $P_t$ (top), EMF (middle), and iso (bottom). . . . .	52
5.2	Distributions of the analysis cuts $P_t$ (top), EMF (middle), and iso (bottom). . . . .	54
5.3	Phi fiducial acceptances as a function of $p_T$ in diphoton MC (top) and data (bottom). . . . .	55
5.4	Di-EM Mass Spectrum. . . . .	57
5.5	Di-EM Mass Spectrum after analysis cuts. . . . .	58
5.6	Distribution of diphoton Monte Carlo overlayed with data. . . . .	59
5.7	$p_T$ distribution of single photons from diphoton Monte Carlo. . . . .	60
5.8	Analysis Cut Efficiencies as a function of Mass (top), $q_T$ (middle), and $\Delta\phi_{\gamma\gamma}$ (bottom). . . . .	61
6.1	Histogram of the Z-mass from the data. . . . .	65
6.2	Distributions of the Phi Width variable in electrons (top), MC photons (middle), and jets (bottom). . . . .	67
6.3	Efficiencies of electrons (top) and jets (bottom) of the Phi Width discrimination variable as a function of $p_T$ . . . . .	68
6.4	Distributions of the CPS_RMS variable in electrons (top), MC photons (middle), and jets (bottom). . . . .	70
6.5	Efficiencies of electrons (top) and jets (bottom) of the CPS_RMS discrimination variable as a function of $p_T$ . . . . .	71
6.6	Distributions of the CPS_RMSSQ variable in electrons (top), MC photons (middle), and jets (bottom). . . . .	72
6.7	Efficiencies of electrons (top) and jets (bottom) of the CPS_RMSSQ discrimination variable as a function of $p_T$ . . . . .	73
6.8	Diphoton events determined by matrix inversion of discrimination variable efficiencies as a function of mass. . . . .	74
6.9	Diphoton events determined by matrix inversion of discrimination variable efficiencies as a function of transverse momentum. . . . .	74
6.10	Diphoton events determined by matrix inversion of discrimination variable efficiencies as a function of opening angle between the two photons. . . . .	75
6.11	Differential diphoton cross-section as a function of mass. . . . .	77

6.12	Differential diphoton cross-section as a function of $q_T$ . . . . .	78
6.13	Differential diphoton cross-section as a function of opening angle. . .	79

# CHAPTER 1

## Introduction

The information provided by this dissertation attempts to extend the knowledge base of the particle physics community. This thesis presents research into the very tiny world of particles and fundamental forces, but focuses on particles that are massless.

Photons are occasionally produced in  $p\bar{p}$  collisions. Direct photon production refers to processes in which the final state photons are produced directly from the hard scattering of incoming quarks and gluons, and not from secondary decays. It is particularly interesting to study photons since their energies and angles are well defined, unlike those of a jet, so that important information can be extracted regarding the underlying fundamental processes. A particularly useful process to examine is that of double photon production, or diphotons. Diphoton production has long been recognized as an important process for testing the parton model, the dynamics of quarks and gluons, and their interactions. In addition, the postulated Higgs boson is theorized to decay into two photons and thus an accurate measurement of the QCD diphoton background is important for any Higgs search.

This analysis presents a measurement of direct diphotons produced at D0. The rate at which direct diphotons occur in proton-antiproton collisions as a function of invariant mass, the diphoton's transverse momentum, and the opening angle between the two photons is revealed. These measurements are performed at higher energies

and with a larger dataset than has ever previously been available. As such, the measurements are made with greater precision and with a larger mass range than in previous analyses.

Chapter 2 provides background and some highlights of particle physics as well as an indication of the importance of this analysis. Chapter 3 briefly describes the Fermi National Accelerator Laboratory's proton-antiproton collider and the D0 detector and some of its intricacies. Chapter 4 gives a description of the dataset and Monte Carlo programs used in this analysis. Chapter 5 explains the identification of photons, electrons, and jets and discusses the analysis cuts, their respective efficiencies, and background suppression. Chapter 6 describes the final steps of the analysis which use a matrix inversion technique. The resulting cross-sections are also presented in this chapter.

# CHAPTER 2

## Theory

### 2.1 The Standard Model

The Standard Model is a theory that describes most particles and forces quite well. It is widely accepted and used by the physics community. The Standard Model describes all matter as being composed of point-like elementary particles called fermions. Fermions have half-integer spin and both quarks and leptons are of this type. Quarks and leptons come in families of three generations each and are listed in Table 2.1 and Table 2.2, respectively.

Generation	Particle (symbol)	Charge (e)	Mass (GeV)
1	Up (u)	+ 2/3	0.0015-0.004
	Down (d)	- 1/3	0.004-0.008
2	Charm (c)	+ 2/3	1.15-1.35
	Strange (s)	- 1/3	0.80-0.130
3	Top (t)	+ 2/3	178.1
	Bottom (b)	- 1/3	4.1-4.4

Table 2.1: Standard Model Quarks [2].

Generation	Particle	Charge (e)	Mass (MeV)
1	Electron ( $e$ )	-1	0.511
	Electron Neutrino ( $\nu_e$ )	0	$< 2 \times 10^{-6}$
2	Muon ( $\mu$ )	-1	105.66
	Muon Neutrino ( $\nu_\mu$ )	0	$< 0.19$
3	Tau ( $\tau$ )	-1	1776.99
	Tau Neutrino ( $\nu_\tau$ )	0	$< 18.2$

Table 2.2: Standard Model Leptons [2].

Quarks are the particles that have fractional charge and make up protons and neutrons. They come in six flavors: up, down, strange, charm, top, and bottom. Particles made of quarks are called hadrons, which are further divided into baryons (containing three quarks) and mesons (containing two quarks). Leptons are particles that have integer charge and do not interact via the strong force. The charged leptons are the electron, muon, and tau, each having a corresponding uncharged neutrino called the electron neutrino, muon neutrino, and tau neutrino. All particles have an antiparticle that has the same characteristics except for reversed charge, and anti-fermions have opposite parity from fermions.

The four fundamental forces, electromagnetic, strong, weak, and gravity, are all mediated or “carried” by particles called vector bosons which have integer spin. The bosons’ characteristics are listed in Table 2.3.

Interaction	Mediating Particle	Rel. Strength	Range (m)	Charge (e)	Mass (GeV)
Strong	Gluon (g)	1	$10^{-16}$	0	0
Electroweak: Electromagnetic	Photon ( $\gamma$ )	$10^{-2}$	$\infty$	0	0
Weak	$W^{\pm}$	$10^{-5}$	$10^{-18}$	$\pm 1$	80.425
	$Z^0$			0	91.1876
Gravity	Graviton	$10^{-39}$	$\infty$	?	?

Table 2.3: Standard Model Gauge Bosons [2, 3].

Particles with electric charge interact via the electromagnetic force, which is mediated by the photon. The weak force is carried by exchange of the  $W$  and  $Z$  bosons. The  $W$  and  $Z$  bosons have large masses compared to the others, and work over short distances. Gravity is theorized to be mediated by the graviton, but no well-developed quantum theory of gravity has yet been proposed, and no evidence of the graviton has yet been discovered. The strong force acts between quarks, works to form baryons, mesons, and holds the nucleus of the atom together. This force is mediated by the gluon. Gluons are chargeless and massless, but do have a different quantum number called color or color-charge. Quarks come in three colors, red, green, and blue, while antiquarks come in cyan (antired), and magenta (antigreen), yellow (antiblue). Only particles whose elementary particle color combinations are white or colorless are allowed to freely exist. As such, particles containing three quarks are composed of quarks where each has a different color (i.e. red, green, and blue) and particles containing two quarks are composed of a quark color-anticolor pair.

Although the Standard Model is not complete, a completely new theory is not expected. Due to much experimental testing confirming its predictions, only extensions of it are expected.

## 2.2 QCD and Higgs Searches

### 2.2.1 QCD and the Requirement of Color

Quantum Chromodynamics (QCD) is the theory that predicts interactions due to the strong force. This thesis studies events containing direct diphotons in proton-antiproton collisions, and are a direct result of the strong force interaction. Basically, protons and antiprotons are each a container of three quarks. These quarks exchange gluons as necessary to maintain a bound, stable state. Since gluons and quarks carry color, they can couple to themselves and can emit gluons. One feature of the strong force is that as the energy of a collision increases, the interaction strength of the strong force gets weaker and minimizes the chance of quarks and gluons to radiate. As such, a collision between proton and antiproton containers is considered to be an interaction between just one constituent (quark or gluon) of each. Given, however, that hundreds of particles can be formed by these collisions, a cross-section ( $\sigma$ ) is often calculated as a measurement of how likely a particular interaction will occur, such as a quark and an antiquark producing two photons.

Color is often a new and strange concept for most and can seem completely contrived. Several physical instances actually mandate its existence, however, and a brief overview is provided here. It is not the case that if you grouped millions of red up quarks together that the human eye would see them as red. Color is instead merely a characteristic held by quarks and gluons whose interaction happens to mirror the color theory of light. This characteristic is, however, necessary to resolve the issues of spin and statistics in baryon spectroscopy [4]. For instance, consider the  $\Delta^{++}(1232)$ , which has spin  $\frac{3}{2}$ . This particle is the bound, ground state system of  $uuu$  and should have a totally symmetric wavefunction under exchange of up quark pairs. However, since this particle has spin  $\frac{3}{2}$ , the wavefunction is required to be antisymmetric under exchange of up quark pairs, which is a problem since spin, space, and flavor consid-

erations do not produce an antisymmetric wavefunction. This issue is resolved if the color parameter is introduced as it provides an antisymmetric wavefunction. Other examples exist, including experimental data on  $e^+e^-$  annihilations [4].

### 2.2.2 The Higgs Boson

The Higgs Boson is a particle that is theorized to couple to any particle with mass. This boson comes from the Higgs mechanism, which introduces a field, called the Higgs field, and has a non-zero vacuum expectation value. This mechanism predicts three massive vector bosons ( $Z^0$ ,  $W^\pm$ ), one scalar boson ( $H$ ), and also gives mass to the quarks and leptons. The discovery of spontaneous symmetry breaking and the Higgs mechanism were a major breakthrough toward unifying the electromagnetic and weak forces. The formal mathematics can be found in [4].

The theory of the Higgs mechanism is very successful, but for the theory to continue, the Higgs boson must be discovered. Higgs searches are ongoing at D0 and CDF at Fermilab and will also be performed at the Large Hadron Collider (LHC) being built at CERN in Switzerland. The Higgs is theorized to have a number of decay modes, and their branching ratios are shown in Figure 2.1. One of the decay modes is that of two photons, making this analysis interesting not only as a QCD measurement, but also for measuring the  $\gamma\gamma$  background for future Higgs searches.

## 2.3 Direct Diphotons

While the Higgs boson is expected to have a two photon decay channel, two photons may also be directly produced in a number of other interactions as shown in Figure 2.2. Direct diphotons and the mechanisms by which they are produced are sensitive to the gluon distribution of the proton and are an excellent method for testing both perturbative and non-perturbative QCD. This thesis includes events from all direct

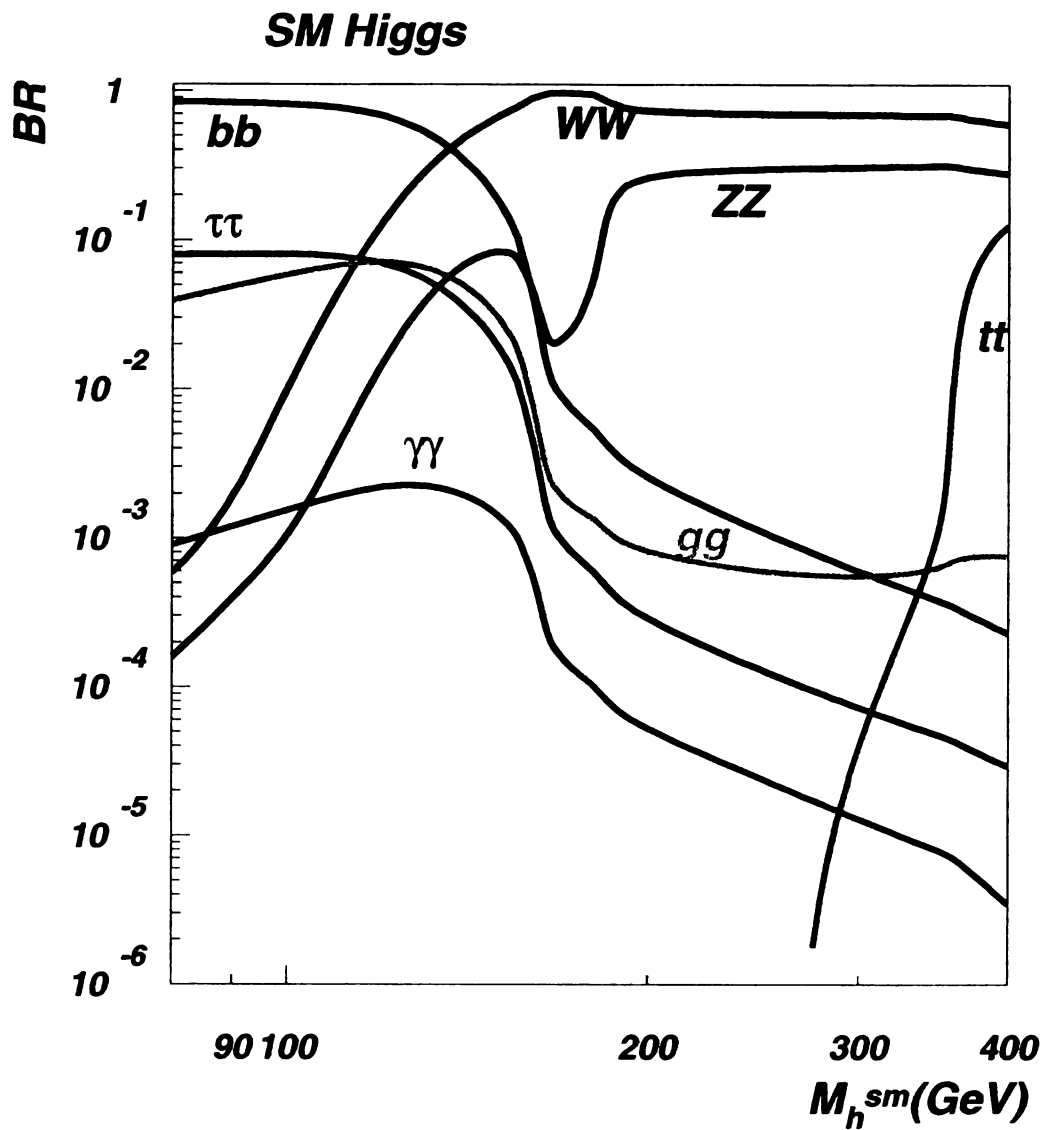


Figure 2.1. Branching ratios of the dominant decay modes of the Standard Model Higgs boson.

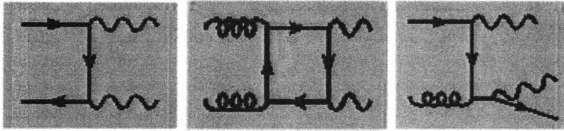


Figure 2.2. Leading order (LO) Feynman diagrams for direct diphoton production in QED, QCD, and mixed.

diphoton processes. The contributions shown in Figure 2.2, are only the leading order processes for direct diphoton production, and therefore the radiative corrections should also be mentioned, and are shown in Figure 2.3. In the Feynman diagrams, the straight lines represent quarks, the wavy lines represent photons, and the curly lines represent gluons. A few other diagrams that include photons due to fragmentation do exist and are sometimes included in theory calculations [6], but the cuts used in this analysis inevitably suppress those contributions.

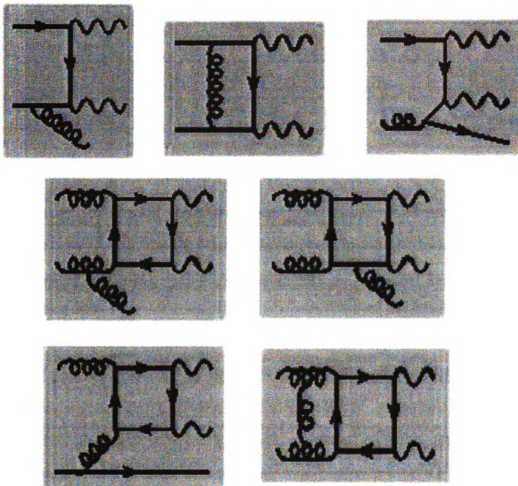


Figure 2.3. Radiative corrections to the LO Feynman diagrams.

# CHAPTER 3

## Fermi National Accelerator

## Laboratory and the D0 Experiment

This chapter will provide a brief description of Fermi National Accelerator Laboratory (Fermilab or FNAL) , the D0 detector, giving more emphasis to the detector subsystems that are pertinent to this analysis, as well as the trigger and data acquisition (DAQ) systems.

### 3.1 Fermilab

Fermilab is the site of the world's, currently, highest energy particle accelerator, the Tevatron, and also is home to a few high energy physics experiments including D0, CDF, and MINOS. Fermilab was commissioned by the U.S. Atomic Energy Commission on November 21, 1967. It is located in Batavia, IL, 40 miles west of Chicago, on what used to be the village of Weston and covers 6800 acres of farmland [7]. Originally named the National Accelerator Laboratory, it was renamed in 1974 in honor of Enrico Fermi, the 1938 Nobel Prize recipient for his work on the artificial radioactivity produced by neutrons, and for nuclear reactions brought about by slow neutrons [8]. Fermilab also holds facilities for cancer treatment, science outreach, and a herd

of American bison that produces calves each year — always a popular attraction for visitors. The Tevatron itself is a particle accelerator ring that has a circumference of 4 miles, and collides protons and anti-protons at a center-of-mass energy of  $\sqrt{s} = 1.96$  TeV. The Tevatron Collider has been run for two major periods of operation, referred to as Run I and Run II. Run I lasted from 1992 to 1996, at which time the Tevatron was shut down for upgrades to both the Tevatron itself and to the detectors that it serves. The data presented in this analysis are from the Run II portion of the D0 experiment which started recording data in March 2001.

## 3.2 Accelerator and Antiproton ( $\bar{p}$ ) Production

Fermilab uses a series of accelerators to generate the proton and antiproton beams that are collided. The information about the accelerator process is based on [9] and [10]. This process starts with tanks of hydrogen gas and the Cockcroft-Walton pre-accelerator. The hydrogen, consisting of one electron and one proton, is ionized to have two electrons, and then accelerated to 750 keV. The  $H^-$  ions then enter the 500 ft. linear accelerator (or LINAC) and are accelerated to 400 MeV using quickly oscillating electric fields that also cause the protons to be grouped into bunches. Once the ions are accelerated, they pass through a carbon foil that strips off the electrons, leaving only protons to continue to the next stage. These protons then travel 20 feet below the surface to the Booster (a synchrotron), where magnets force them to travel in a circle and accelerate them up to 8 GeV, where they are then passed to the Main Injector.

The Main Injector accelerates these protons to 120 GeV. A few of these continue to be accelerated to 150 GeV and injected into the Tevatron, while the rest are sent to the antiproton source. Those that are sent to the anti-proton source collide with a fixed nickel target where a wide variety of particles are produced, one of

which is the antiproton. For every million protons that hit the target, about 20 antiprotons are produced. The antiprotons that are produced are focused into a beam using a lithium lens, and passed through a pulsed magnet, acting as a charge-mass spectrometer, that removes the particles that are not antiprotons. Now, since the protons strike the nickel target at the same time the antiprotons that are produced have a small variation (or width) in time, but a large width in energy since they can be produced at different energies. So, these are now sent to the Debuncher where radio-frequency (or RF) cavities are used to exchange the energy and time widths, creating a continuous (instead of bunched) beam of antiprotons of similar energy. This antiproton beam is diffuse due to the different, random angles at which they are produced. This randomness can be likened to temperature. It is important to remove the diffuseness and focus the beam in order to increase the probability of producing rare particles in the collider. To accomplish this, the beam is “cooled” using a method called Stochastic Cooling. The beam is then sent to the Accumulator where the beam is further focused and the antiprotons are stored and re-bunched. Once enough antiprotons are produced (which takes several hours), they are sent back to the Main Injector, accelerated to 150 GeV, and injected into the Tevatron in the opposite direction of the protons signaling a new “store” of 36 bunches of protons and 36 bunches of antiprotons.

Once in the Tevatron, the proton and antiproton beams are accelerated to almost 1 TeV, and have a speed nearly that of light. The beams are kept in a helical orbit around the ring by a 4.2 T magnetic field created using about 1000 superconducting magnets cooled, using liquid helium, to 4.3 K. The beams are then steered so the bunches cross each other every 396 ns producing collisions at two interaction locations, one of which is centered in the D0 detector.

# FERMILAB'S ACCELERATOR CHAIN

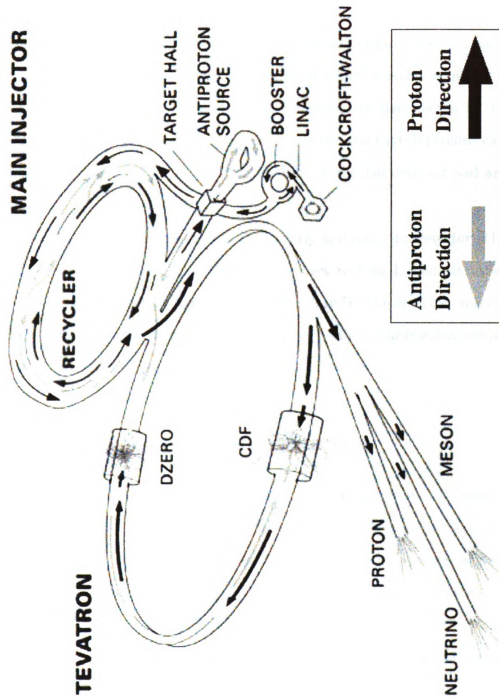


Figure 3.1. Layout of Fermilab's accelerators [9].

### 3.3 The D0 Detector

Most of the collisions that happen every 396 ns are glancing collisions that produce uninteresting results. Sometimes, however, a head-on collision or hard scatter occurs between one parton of the proton (a part of the proton which is either a quark or gluon) and one parton of the antiproton. In these collisions, the partons not in the collision travel down the uninstrumented beam pipe, but the two that did collide can annihilate and produce new particles that travel through the D0 detector and are studied.

The D0 detector, pictured in Figure 3.2, is a nearly-hermetic,  $4\pi$  detector [11]. Portions of the detector are completely new with respect to Run I, whereas other portions have been recycled and are again being used in Run II. The detector consists of several subdetectors that are layered like an onion or parfait. These subdetectors are each designed to measure different traits of particles.

### 3.4 Coordinate System and Variables

The D0 detector uses a right-handed coordinate system with the origin at its geometric center. The positive z-axis is defined to be in the direction of the protons, and the positive y-axis is upward. The angles  $\theta$ , and  $\phi$ , are the polar and azimuthal angles, respectively, with the  $\theta = 0$  defined along the beam line and  $\phi = 0$  along the x-axis [12].

For relativistic particles, it is natural instead of using  $\theta$ , to use the Lorentz invariant variable rapidity,  $y$ , defined as

$$y = \frac{1}{2} \ln \left( \frac{E + p_z}{E - p_z} \right) \quad (3.1)$$

for finite angles in the limit that  $\lim \frac{m}{E} \rightarrow 0$  [12]. This variable is more convenient to

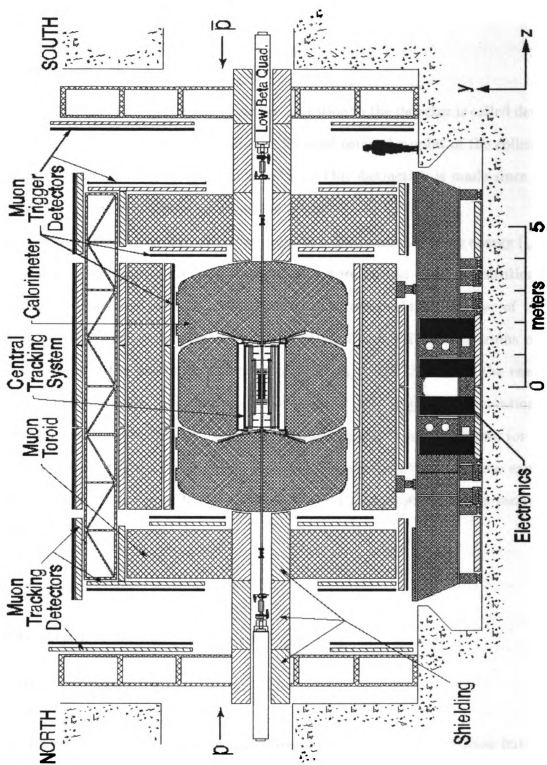


Figure 3.2. The D0 Detector [11].

use when approximated by the pseudorapidity,  $\eta$ , defined as

$$\eta = -\ln\left(\tan\frac{\theta}{2}\right). \quad (3.2)$$

Pseudorapidity calculated from the origin to a position in the detector is called detector  $\eta$ , or  $\eta_{det}$ , whereas the pseudorapidity calculated using the point of the collision, or primary vertex, is the physics  $\eta$ , or simply  $\eta$ . This distinction is made since the primary vertex does not always occur at the origin.

While the proton-antiproton collisions occur at a fixed center-of-mass energy ( $\sqrt{s}$ ), these protons and antiprotons have a parton structure due to their constitution of a number of subatomic particles. This parton structure prohibits the use of total conservation of energy principles in the analysis since the individual partons only carry a fraction of the proton/antiproton's total energy, with the rest of the energy escaping down the beam pipe with the other partons [13]. Instead, conservation of momentum and conservation of energy are applied in the transverse plane (or the plane perpendicular to the beam pipe). This may be used since the transverse energy and momentum balance prior to the collision are zero. Consequently, useful variables are defined:

- Transverse Energy,  $E_T = E \sin \theta$
- Transverse Momentum,  $p_T = p \sin \theta = \sqrt{p_x^2 + p_y^2}$
- Missing Transverse Energy,  $\cancel{E}_T$ .

$\cancel{E}_T$  occurs when a particle, such as a neutrino, is produced in the collision but not found by the detector, and thus carries away some amount of energy. When energy conservation in the transverse plane is performed, the total does not sum to zero revealing this missing transverse energy.

## 3.5 Tracking System

The tracking system of the detector, pictured in Figure 3.3, is completely new for Run II and is designed to detect charged particles as well as locate the primary vertex with a precision of  $35\mu\text{m}$ . The tracking system consists of the Silicon Microstrip Tracker (SMT), the Central Fiber Tracker (CFT), and is surrounded by a solenoidal magnet with magnetic field strength of 2T [11]. The magnetic field will cause a charged particle's path to deflect in a circle allowing its momentum to be measured. The equation that predicts this phenomenon is

$$r = \frac{p_T}{qB} \quad (3.3)$$

where  $r$  is the radius of curvature,  $p_T$  is the transverse momentum,  $q$  is the charge, and  $B$  is the magnetic field strength.

### 3.5.1 Silicon Microstrip Tracker

The SMT provides tracking and vertexing information over a pseudorapidity range of  $-3 < \eta < 3$ . Given that the primary vertex does not always occur at the origin and some particles decay after a short distance creating secondary vertices, a combination barrel-disk design for the SMT, pictured in Figure 3.4, was employed. In this design, the barrel portions and the CFT detect particles of low  $\eta$ , and the disks detect particles with high  $\eta$ . The SMT consists of six barrels, and each barrel has four silicon readout layers. Each layer is composed of silicon modules known as ladders. The ladders are mechanical support structures made of silicon with beryllium strips that aid in alignment with carbon-boron fiber/Rohacell rails that bridge the beryllium strips. All of the barrels use p-type axial sensors and n-type stereo silicon sensors. Layers one and three of the four inside barrels use  $90^\circ$  stereo, double-sided silicon sensors,

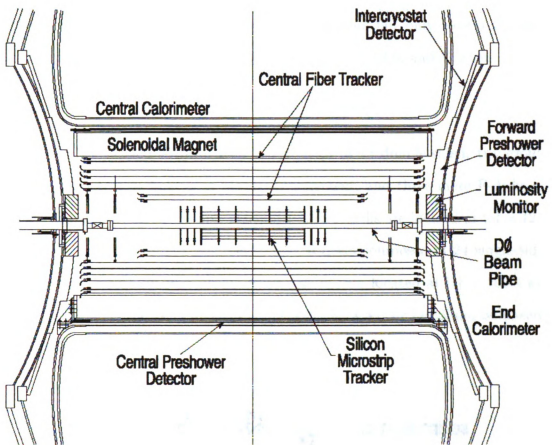


Figure 3.3. Cross-section of the D0 tracking system [11].

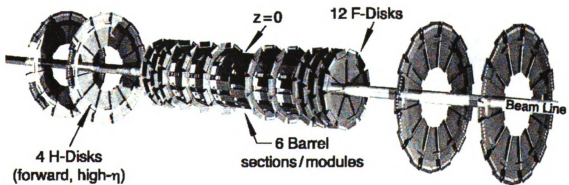


Figure 3.4. Barrel/Disk design of the SMT [11].

while the outer two barrels use single-sided sensors in these layers. Layers two and four of all of the barrels use double-sided silicon sensors but only have a  $2^\circ$  stereo offset. The centers of the barrels are located at  $|z| = 6.2, 19.0,$  and  $31.8$  cm.

Each barrel is capped with an F-disk composed of 12 double-sided, trapezoidal shaped, wedge detectors built in a planar arrangement, and three more F-disks are placed at each end of the barrel-disk assembly. The F-disks are located at  $|z| = 12.5, 25.3, 38.2, 43.1, 48.1,$  and  $53.1$  cm. Next, four H-disks composed of 24 single-sided wedge detectors, also built in a planar arrangement, are located at  $|z| = 100.4$  and  $121.0$  cm for high  $\eta$  coverage. Finally, all of this is supported by beryllium bulkheads.

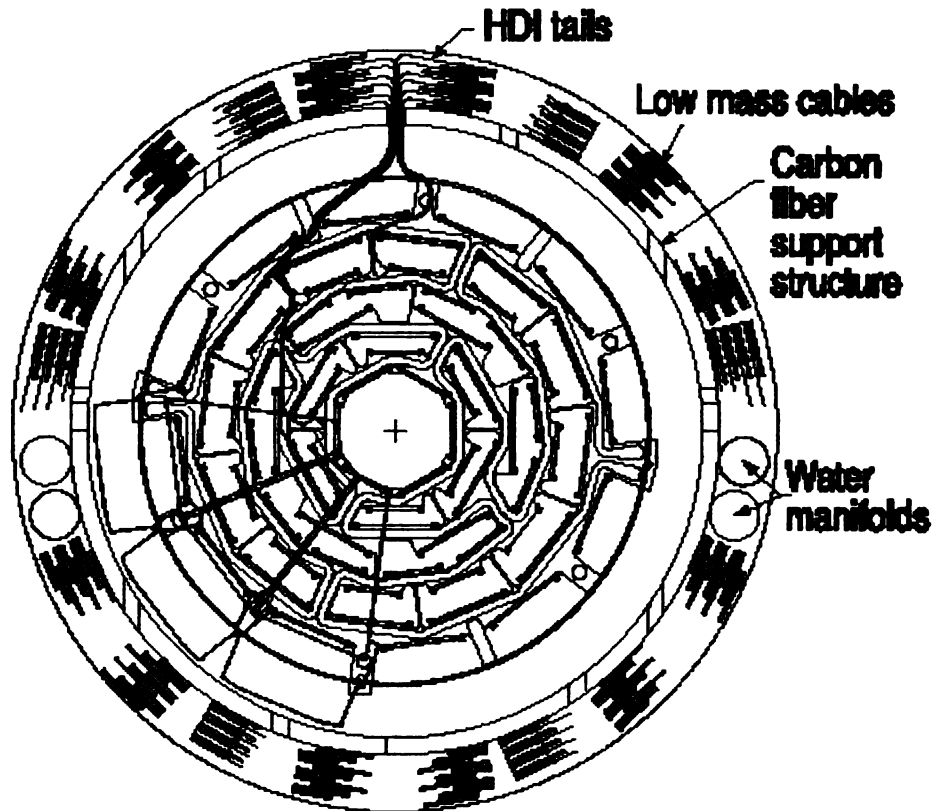


Figure 3.5. Cross sectional view of the SMT [11].



Figure 3.6. Positioning of two fiber ribbons to form a doublet [11].

These bulkheads are designed to support the ladders and disks as shown in Figure 3.5, as well as allow support for signal readout cables and coolant. All of these detectors operate at a temperature below  $5^{\circ}\text{C}$  [11].

### 3.5.2 The Central Fiber Tracker

The CFT is the second portion of the tracking system and surrounds the SMT. The CFT is composed of about 77,000 scintillating fibers positioned on eight concentric cylinders (made with a core of Rohacell and coated with linear carbon fibers impregnated with 40% resin) and fills the space from 20-52 cm from the center of the beam line. The inner two cylinders are only 1.66 m long to allow space for the SMT H-disks, while the other six cylinders are 2.52 m long.

The scintillating fibers are arranged into ribbons of 128 fibers each. Two of these ribbons are formed into a doublet by positioning the second layer in the interstitial spaces of the first, pictured in Figure 3.6. Each cylinder contains one axial doublet ribbon oriented along the beam path and one stereo doublet ribbon of either  $u$  or  $v$  oriented at  $\pm 3^{\circ}$ . These stereo layers start on the inner cylinder with a  $u$  layer, and alternate for each cylinder. The scintillating fibers are 835 microns in diameter. This small diameter provides a doublet resolution of 100 microns. The fibers are made of polystyrene doped with fluorescent dyes of 1% paraterphenyl that emits light at 340 nm, and, due to paraterphenyl's low mean free path in polystyrene, a secondary wave-shifter dye of 3-hydroxyflavone at 1500 ppm that absorbs the 340 nm light and

emits 530 nm light that transmits well through the polystyrene. These fibers are then doubly clad with polymethylmethacrylate and then fluoro-acrylic. The dual claddings provide for both better optical and mechanical performance. One end of the fibers is capped with an aluminum coating that provides a reflectivity of 90%. The other end is connected to waveguides pictured in Figure 3.7, whose composition is the same as the fibers except for the dyes, which pipe out the light from the detector for readout [11]. The waveguides are connected to Visible Light Photon Counter (VLPCs) cassettes that are immersed in a liquid helium cryostat and turn the light from the CFT into electrical signals. The VLPCs operate at 9 K, have a quantum efficiency of  $> 75\%$ , a gain of 22,000 to 65,000, and are able to detect single photons [11]. The  $p_T$  resolution at  $\eta_{det} = 0$  of the entire tracking system can be parameterized as  $\sigma_{p_T}/p_T = \sqrt{0.0015^2 + (0.0014p_T)^2}$  [11].

### 3.6 Preshower

The preshower detectors, also new for Run II, are the next layer of the detector after the SMT, CFT, and the magnetic field producing solenoid. The preshower is designed to improve photon and electron identification, enhance tracking and calorimetry matching, and help correct electromagnetic energy measurement offline due to the uninstrumented solenoid, a lead radiator (which, combined, is about two radiation lengths in thickness), and other material such as structural support and readout cabling. It is divided into three portions, the central preshower (CPS) and the two forward preshower (FPS) detectors. Both the CPS and FPS are made of triangular strips of scintillator with a wavelength-shifting fiber in the center and then coated with two layers of mylar to increase light yield. The fibers are read out by VLPCs similar to the CFT. The triangular strips are arranged so that no dead space exists between them. The CPS and FPS detectors are made from the same material, but

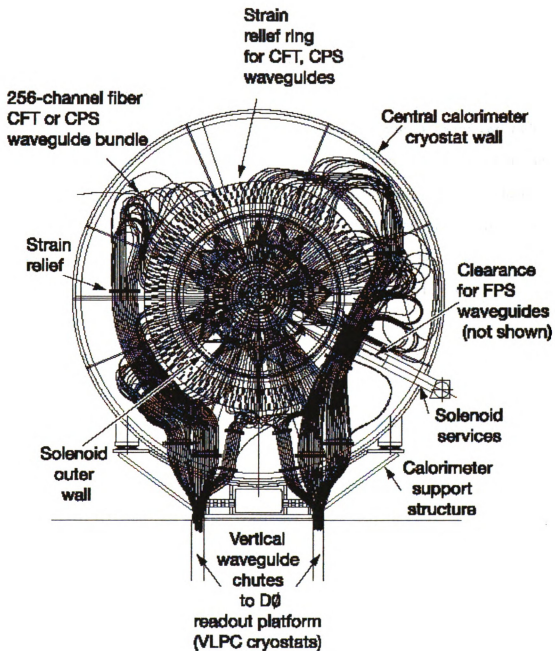


Figure 3.7. Cross sectional view of the CFT and associated waveguides [11].

their geometries, pictured in Figure 3.8, are a little different.

The CPS detector is composed of three layers of the scintillating strips and is positioned in the 5 cm gap between the solenoid and the central calorimeter. The three layers are in an axial, u, and v geometry with the u-layer at a stereo angle of  $23.774^\circ$  and the v-layer at a stereo angle of  $24.016^\circ$ , and have 1280 strips each [11].

The two FPS detectors are positioned on the heads of the calorimeter endcaps. Each FPS detector is made of two layers of the triangular strips, a two radiation length thick layer of lead-stainless-steel absorber, and two more layers of triangular strips. The inner layers are called the MIP (minimum-ionizing particle) layers and the outer layers are called the shower layers. This is due to the inner layers typically detecting charged MIPs, and the outer layer also detecting particle showers produced in the absorber. These detectors are also read out using the VLPCs.

### 3.7 Calorimeter

The D0 calorimeter system, shown in Figure 3.9, is unchanged from Run I. It is designed to provide very accurate energy measurements for electrons, photons, and jets. It is a compensating-sampling calorimeter that consists of three portions, the central calorimeter (CC), and two endcap calorimeters (EC). (It is called a “compensating-sampling” because the calorimeter collects only a sample of a particle’s energy, but is considered compensating since uranium releases extra energy by fast neutron fission during a particle’s shower.) The CC covers  $|\eta_{det}| < 1.2$  and the ECs extend the coverage up to  $|\eta_{det}| \approx 4$ . In the  $\phi$ -dimension, the calorimeter consists of 32 separate modules with unavoidable gaps between them. These gaps, often referred to as phi-cracks, make it possible for particles to both escape through them, and be mis-measured if their position is too close to the edge of the modules. All three portions of the calorimeter are made of three distinct sections: an electromagnetic (EM) section,

a fine hadronic (FH) section, and a coarse hadronic (CH) section made of plates of metal to act as absorbers. The EM section of the CC uses 3 mm thick and the EC uses 4 mm thick plates of pure depleted uranium,  $^{238}\text{U}$ . The fine hadronic sections are made of 6 mm thick plates of uranium-niobium (2%) alloy, and the coarse hadronic sections use 46.5 mm thick plates of copper in the CC and stainless steel in the EC. The calorimeter uses liquid argon at a temperature of 90 K as the active material that fills the space between the plates.

The absorbers cause particles produced from the collision to shower into secondary particles at a geometric rate as they interact with the absorber atoms. Electromagnetic objects, namely photons and electrons, lose energy by traveling through matter primarily by two shower processes: bremsstrahlung ( $e \rightarrow e\gamma$ ) (literally braking radiation) and pair production ( $\gamma \rightarrow e^+e^-$ ). As these showers occur, the secondary particles ionize the argon atoms which are collected and provide a measurement of the original particle's energy, given that

$$E(x) = E_0 e^{-\frac{x}{X_0}} \quad (3.4)$$

where  $x$  is the distance traveled, and  $X_0$  is the radiation length of the material through which it travels.  $X_0$  is defined for electrons as the mean distance over which the electron will lose  $\frac{1}{e}$  of its energy through the bremsstrahlung process, and defined for photons as the thickness of material through which a photon travels so that the probability of its converting to an electron-positron pair is equal to  $7/9$ , provided that the energy of the photon is of order 1 GeV [14]. The radiation length for uranium is approximately 0.34 cm [16]. Due to the nature of EM objects, the calorimeter is designed with four layers of uranium plates aptly called EM1, EM2, EM3, and EM4

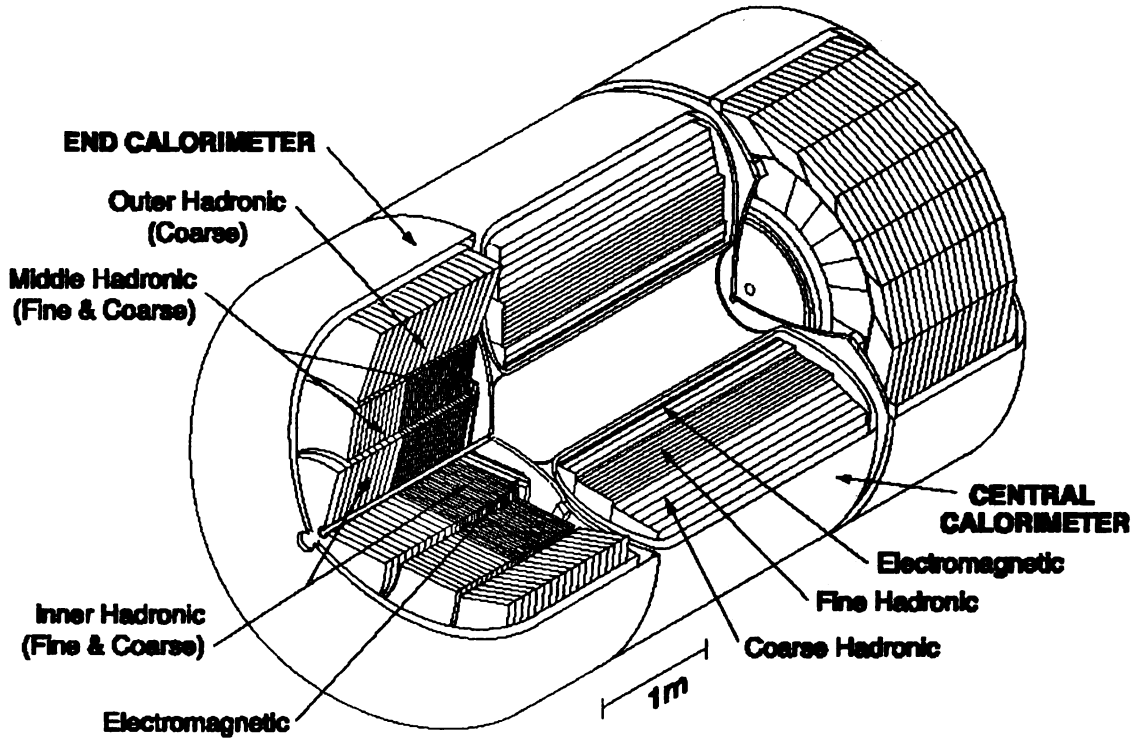


Figure 3.9. D0 calorimeter [11].

which extend radially outward from the beam pipe where these objects will deposit most of their energy in a narrow shower.

Hadrons (particles often present in jets), however, interact differently than EM objects. Hadrons interact with the uranium nuclei through the strong force and have an associated quantity similar to radiation length, called nuclear interaction length,  $\lambda$ . Nuclear interaction length is defined as the mean free path between inelastic interactions, and is calculated by

$$\lambda^{-1} = N_A \sum \frac{w_j \sigma_j}{A_j} \quad (3.5)$$

where  $N_A$  is Avogadro's number and  $w_j$  is the weight fraction of the  $j$ th element in the element [16]. These hadrons typically break up into other particles as well as

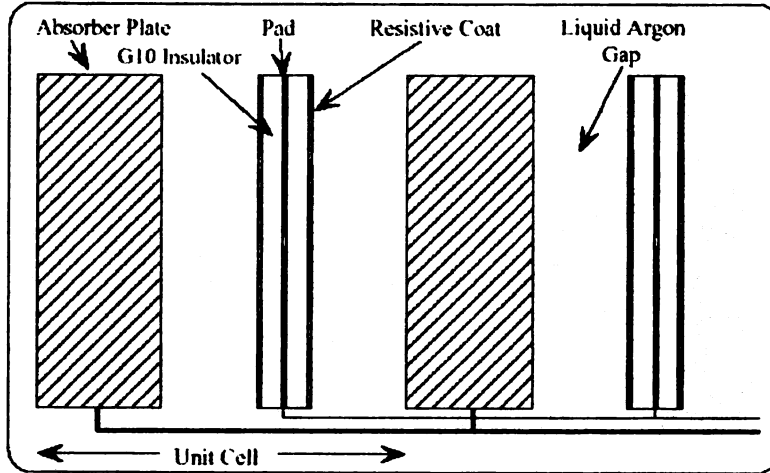


Figure 3.10. Calorimeter unit cell [17].

causing the uranium atoms to fission. This leads to larger showers in both width and length in the calorimeter. Layer depths for the EM, FH, and CH, are shown in Table 3.1.

	EM	FH	CH
CC depth	1.4, 2.0, 6.8, $9.8X_0$	1.3, 1.0, $0.76\lambda$	$3.2\lambda$
EM depth	1.6, 2.6, 7.9, $9.3X_0$	1.1, 1.1, 1.1, $1.1\lambda$	$3.2\lambda$

Table 3.1: Depths of the calorimeter layers.

All of these layers are instrumented to create readout cells of size  $0.1 \times 0.1$  in eta-phi space, with the exception of the EM3 layer. This layer is further divided into  $0.05 \times 0.05$  to increase EM shower precision in position.

Each cell, pictured in Figure 3.10, is made of an absorber plate, a gap filled with liquid argon, a G-10 sheet coated with copper and then by an insulating epoxy, another gap of liquid argon, another absorber plate, and so on. As each particle passes through the detector, it starts a shower of particles inside the absorber plate

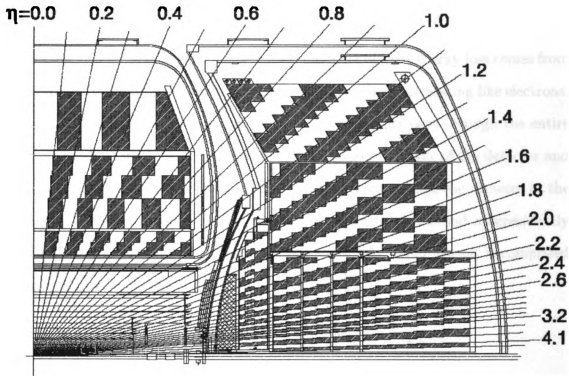


Figure 3.11. Pseudo-projective geometry and segmentation pattern of the calorimeter.

producing many secondary particles. The secondary particles proceed to ionize the liquid argon. The ionized electrons are then attracted to the G-10 sheet due to an electric field generated by grounding the absorber plates, and placing a positive high voltage on the G-10 sheets. The electron drift time across the 2.3 mm liquid argon gap is about  $450 \mu\text{s}$  [11]. The drifting electrons induce an image charge on the copper which is read out as the signal.

The cells of each layer are aligned and grouped to form pseudo-projective towers, as shown in Figure 3.11. These are considered pseudo-projective because the centers of the cells lie on rays projecting from the center of the calorimeter, but the cell edges are perpendicular to the absorber plates. These towers are also aligned in the approximate direction of shower development.

## 3.8 Muon System

Muons are much more massive than electrons and most of their energy loss comes from interaction with the detector material rather than from bremsstrahlung like electrons. Because of this behavior, muons above  $\approx 3.5$  GeV typically pass through the entire calorimeter, which is why the muon system is the outermost layer of the detector and is well protected from debris from the hadronic and electromagnetic showers in the calorimeter. The D0 muon system is intended to identify muons and independently measure their momenta in a toroidal magnetic field. The muon system is comprised of three main components:

- Wide Angle MUon Spectrometer (WAMUS) covering  $|\eta| < 1$
- Forward Angle MUon Spectrometer (FAMUS) covering  $1 < |\eta| < 2$
- Solid-iron magnet forming a toroidal field of 1.8 T.

The WAMUS has three layers of proportional drift tubes and two layers of plate scintillation counters that help with triggering and removal of background muons from cosmic rays. The FAMUS has three layers of mini-drift tubes and three layers of scintillation pixel counters that help with triggering [18]. More information on this system can be found in [11] and [18].

## 3.9 Luminosity Monitor (LM)

D0 has two luminosity detectors mounted at  $z = \pm 140$  cm on the outer surface of the endcaps and are positioned in the area between the beam pipe and the FPS (pictured in Figure 3.3). These detectors monitor the luminosity at the D0 interaction region by detecting inelastic  $p\bar{p}$  collisions [11]. The LM detectors constitute two arrays of scintillation counters, are 15 cm long, and cover  $2.7 < |\eta| < 4.4$ . Luminosity is a

quantity that can be described to the layperson as the amount of data recorded. To the physicist, however, luminosity,  $\mathcal{L}$ , is given by

$$\mathcal{L} = f \frac{\bar{N}_{LM}}{\sigma_{LM}} \quad (3.6)$$

where  $\bar{N}_{LM}$  is the average number of inelastic collisions per beam crossing,  $f$  is the beam crossing frequency, and  $\sigma_{LM}$  is the effective cross section.

### 3.10 Trigger System and DAQ

As stated previously, the proton and anti-proton beams cross every 396 ns which equates to 2.5 million crossings every second (2.5 MHz). Most of these events consist of glancing collisions and are considered uninteresting by today's standards. Considering this and the amount of data space required per event, it would be wildly inefficient to record every event. This is where the Trigger System and the Data Acquisition come into play by saving and writing to tape only the events that are deemed interesting.

The D0 trigger has three distinct levels of decision and, overall, was designed to reduce 7 MHz of input rate to 50 Hz written to tape, as illustrated in Figure 3.12. The trigger decisions are made looking for certain signatures in the detector that correspond to different objects or events. Each level allows fewer events to pass than the previous by examining events in more detail and consequently taking a little more time. For example, an EM event trigger might require two detector sections (or towers) with at least 6 GeV deposited in each tower's EM layers at Level 1, require one of those detector towers and its neighboring towers (or cluster) to have at least a total of 15 GeV deposited in the EM layers at Level 2, and require that cluster to be completely reconstructed to an EM physics object of at least 35 GeV at Level 3, but

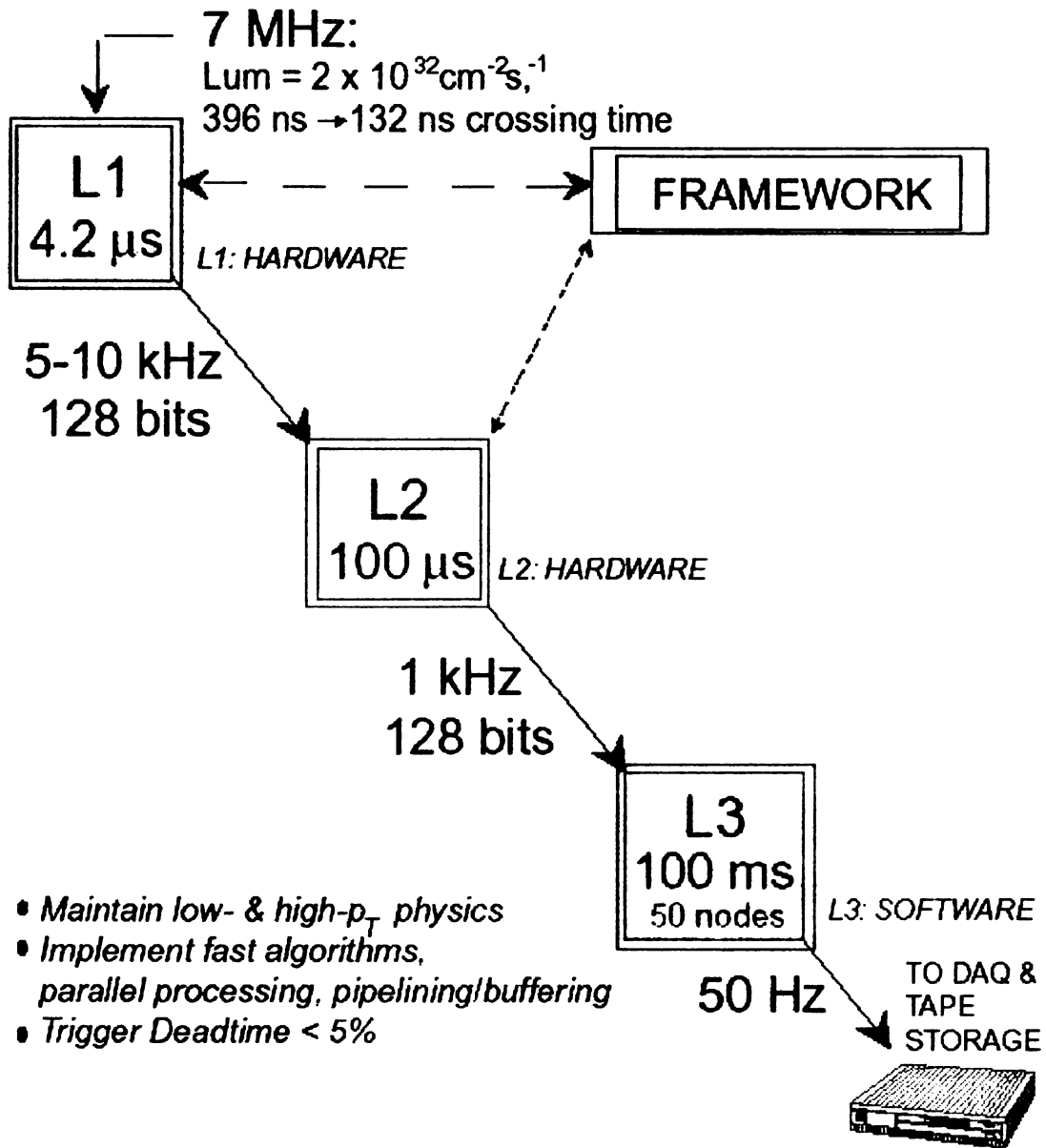


Figure 3.12. Designed D0 trigger scheme[17].

veto on events containing hadronic objects and events with only one EM object.

### **3.10.1 Level 1 Trigger**

The first level (L1) is composed of a hardware trigger consisting of Field Programmable Gate Arrays (FPGAs) holding short algorithms in order to make quick decisions since it must do so for every beam crossing. These algorithms view the detector in a very coarse fashion only using calorimeter towers, for example, instead of actual physics objects. At L1, only the calorimeter, CFT, muon system, and luminosity monitor portions of the detector are used. The information from these detectors is read into the trigger framework, and based on a maximum of 128 different And/Or trigger terms, or trigger bits, the event is either rejected and dumped, or it is passed onto level 2.

### **3.10.2 Level 2 Trigger**

The second level (L2) consists of preprocessors for each detector subsystem that combine signals from the system into physics objects. It no longer views information in terms of calorimeter towers and hits in the tracker, but rather electromagnetic objects and tracks. L2 also contains global processors (L2Global) that can look at these objects on an event wide basis. This level contains both hardware and software algorithms referred to as firmware. L2 was designed to take up to 10 kHz input with a maximum acceptance rate of 1 kHz.

### **Level 2 Global**

L2Global is responsible for making trigger decisions based on the physics objects created by each subsystem's preprocessors. These decisions can be made based solely on the objects themselves or by combining objects from different systems. For exam-

ple, it can make a decision based on a muon object itself, or it can decide based on whether a muon object has a spatially matched track object as well.

The decision process begins by examining which of the 128 bits fired in L1. Each L1 bit has an associated L2 script that contains a number of filters and a minimum number of global objects to pass each filter. These global objects are made from tools. Tools are specific C++ classes that build objects based on selection criteria that decide which from the list of L2 preprocessor objects should be made into global objects. These tools are also where objects from different preprocessors can be combined into a single global physics object. An example of a script requires two EM objects greater than 7 GeV with matched STT tracks and one EM object with isolation less than 0.2. If any L2 script passes, the event is passed to level 3.

### **3.10.3 Level 3 Trigger**

The third level (L3) is a completely programmable software trigger that is designed to reduce 1 kHz of input rate to 50 Hz to be recorded to tape for offline analysis. This trigger is run on a collection of Linux based computers, or Linux farm, that processes the events in parallel [11]. At L3, the software constructs the physics objects into photons, electrons, muons, taus, jets, vertices, and missing energy, as well as the relationships between them like azimuthal angle and invariant mass. One or more L3 scripts each containing filters are assigned to each L2 bit that fires and is compared to a programmable trigger list. If the event is accepted, it is then written to tape.

### **3.10.4 Data Acquisition (DAQ)**

There are a great many detectors and electronic systems in this experiment, as previously outlined. A program called COOR controls the systems and is used for DAQ. COOR performs everything from calibration to synchronizing the systems to actually

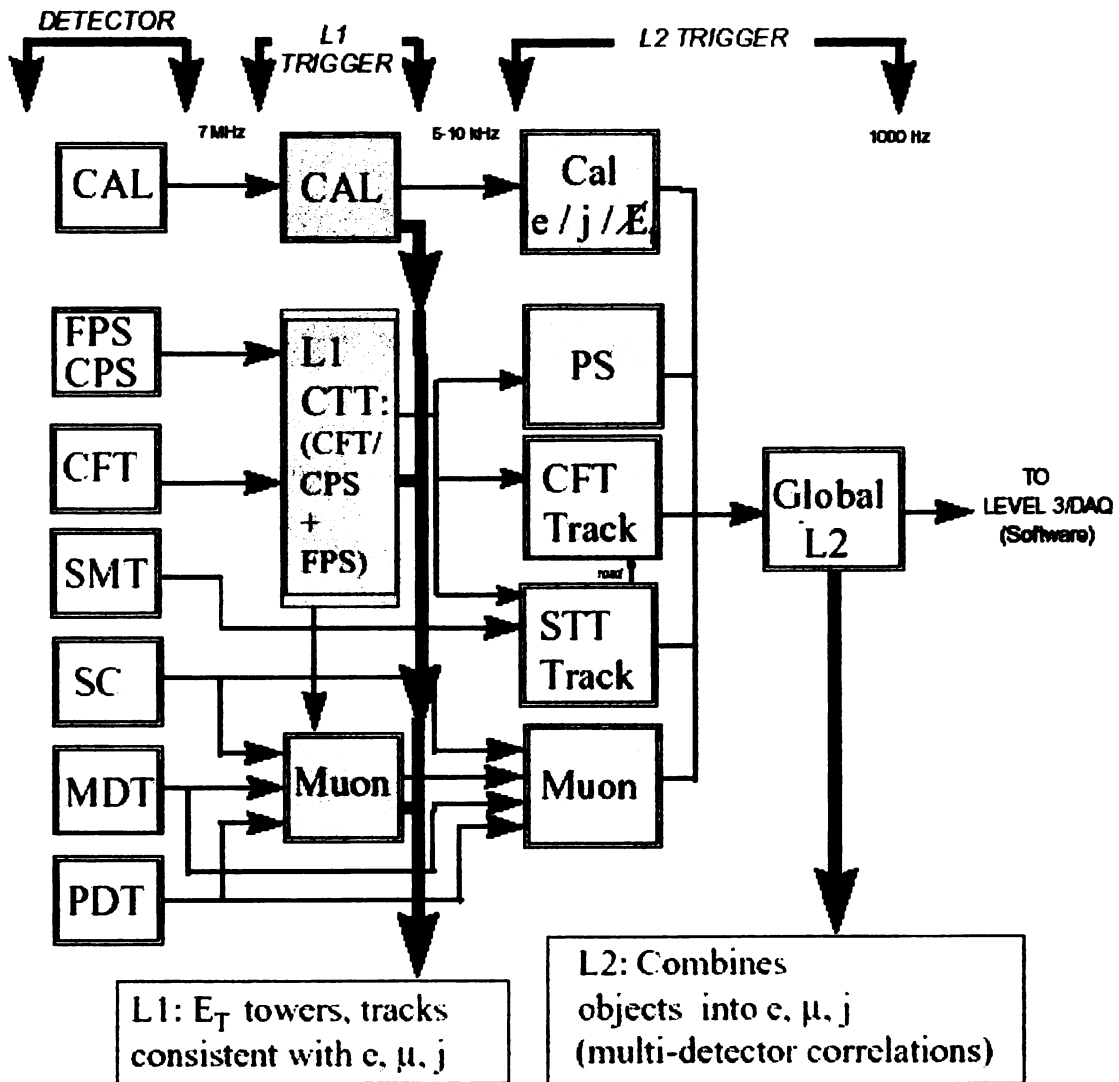


Figure 3.13. L1 and L2 trigger flow [17].

recording the data. All of these detector systems also have monitoring systems to ensure that they are running properly and the data are not compromised. The monitoring systems and COOR are controlled by physicists around-the-clock on a shift schedule whenever a store of protons and anti-protons is in the Tevatron.

### 3.11 DORECO and CAF

After an event is written to tape, the entire event is reconstructed for use in analysis. This is done by the DORECO program on many farms of computers. DORECO uses all of the information from the detector not only to reconstruct all of the particles detected in an event, but also to trim down their associated variables to a bare-bones format called thumbnails (or TMBs) for ease in handling and hard-drive space considerations for the analyst. The specifics of the reconstruction algorithms relevant to this analysis are discussed later in Section 5.1. These TMBs are stored in the sequential access via metadata (SAM) data handling system. All of the data are then skimmed by the Common Samples Group (CSG) at D0 into separate datasets that group similar events together. Examples of this would be events that contain two electromagnetic objects of high  $p_T$ , or events that contain 3 jets. The events are also processed into a format that is designed to be universal for all collaborators at D0 called CAF (Common Analysis Format).

CAF is a set of C++ classes and scripts that allow the users to create a ROOT-based file to access all the variables they need including likelihoods and matrix algorithms designed by other users [19]. This allows for users to share their work so that everyone does not have to design their own methods. It also, however, provides the ability to access only the variables they need, thus, writing only the variables of interest. For example, this analysis is principally concerned with photons, and therefore, does not require information regarding the muons.

# CHAPTER 4

## Dataset and Monte Carlo

This chapter will explain the triggers used to collect the data used in this analysis, and the Monte Carlo samples used to simulate expected results. It will also describe the size of the data sample and the method that was used to skim the data into different dataset definitions.

### 4.1 Trigger

The events used in this analysis were selected using a number of triggers that fire due to high- $p_T$  electromagnetic objects. This allows for examination of a small subset of all the data collected with the D0 Detector. The triggers used are listed in Table 4.1, and are broken down by trigger list version. Fermilab is continually making improvements to the Tevatron in an attempt to increase the instantaneous luminosity delivered to its experiments by increasing the number of bunches of particles in the ring and by increasing the number of particles per bunch. As these improvements are made, tighter triggers must be employed to keep the recording rate within acceptable limits. For this reason, as well as to make use of better algorithms that collaborators design, D0 must periodically alter the triggers, thus creating different trigger list versions. Each trigger list version has the suite of triggers logically “OR’d” together.

Trigger List	Trigger	L1	L2	L3
v8-v11	EM_HI	CEM(1,10)	-	ELE_LOOSE(1,30)
	EM_HI.SH	CEM(1,10)	-	ELE_LOOSE.SH.T(1,20)
	EM_MX	CEM(1,15)	-	ELE_LOOSE(1,30)
	EM_MX.SH	CEM(1,15)	-	ELE_LOOSE.SH.T(1,20)
	EM_HI.2EM5.SH	CEM(2,5)	-	ELE_LOOSE.SH.T(1,20)
v12	E1.SHT20	CEM(1,11)	-	ELE_NLV_SHT(1,20)
	E2.SHT20	CEM(2,6)	-	ELE_NLV_SHT(1,20)
	E3.SHT20	CEM(2,3) CEM(1,9)	-	ELE_NLV_SHT(1,20)
	E1.SH30	CEM(1,11)	-	ELE_NLV_SH(1,30)
v13	E1.SHT22	CEM(1,11)	L2CALEM(15,x)	ELE_NLV_SHT(1,22)
	E2.SHT22	CEM(2,6)	L2CALEM(15,x)	ELE_NLV_SHT(1,22)
	E3.SHT22	CEM(2,3) CEM(1,9)	L2CALEM(15,x)	ELE_NLV_SHT(1,22)
	E1.SH30	CEM(1,11)	L2CALEM(15,x)	ELE_NLV_SH(1,30)
v14	E1.SHT25	CEM(1,12)	L2CALEM(15,x)	ELE_NLV_SHT(1,25)
	E3.SHT25	CEM(1,12)	L2CALEM(x,11,0.2)	ELE_NLV_SHT(1,25)
	E1.SH35	CEM(1,12)	L2CALEM(15,x)	ELE_NLV_SH(1,35)
	E3.SH35	CEM(1,12)	L2CALEM(x,11,0.2)	ELE_NLV_SH(1,35)
	E1.ISHT22	CEM(1,12)	L2CALEM(15,x)	ELE_NLV_SHT(1,22) IsoEle_SHT(1,22)
	E3.ISHT22	CEM(1,12)	L2CALEM(x,11,0.2)	ELE_NLV_SHT(1,22) IsoEle_SHT(1,22)
	E1.ISH30	CEM(1,12)	L2CALEM(15,x)	ELE_NLV_SH(1,30) IsoEle.SH(1,30)
	E3.ISH30	CEM(1,12)	L2CALEM(x,11,0.2)	ELE_NLV_SH(1,30) IsoEle.SH(1,30)

Table 4.1: Triggers by trigger list.

The notation in Table 4.1, is described by the following:

CEM( $n,x$ ) represents the number of EM trigger towers,  $n$ , with energy of at least  $x$  (GeV).

EM(1,12) requires one EM candidate with energy of at least 12 GeV.

L2CALEM(15, $x$ ) represents an L2 cluster with at least 15 GeV.

L2CALEM( $x,E,0.2$ ) requires a single tower EM object with isolation less than 0.2 and energy of at least  $E$  (GeV).

L2CALDIEM(18) requires the sum of the two highest EM towers to be at least 18 GeV.

ELE\_LOOSE( $n,x$ ) represents the number of loose electron candidates,  $n$ , with energy of at least  $x$  (GeV).

ELE\_LOOSE\_SH\_T( $n,x$ ) represents the number of loose electron candidates,  $n$ , with energy of at least  $x$  (GeV), satisfying transverse shower shape requirements.

ELE\_NLV( $n,x$ ) represents the number of loose electron candidates,  $n$ , with energy of at least  $x$  (GeV).

ELE\_NLV\_SH( $n,x$ ) represents the number of loose electron candidates,  $n$ , with energy of at least  $x$  (GeV), satisfying loose shower shape requirements.

ELE\_NLV\_SHT( $n,x$ ) represents the number of loose electron candidates,  $n$ , with energy of at least  $x$  (GeV), satisfying tight shower shape requirements.

IsoEle\_SHT(1,22) represents one isolated electron candidate satisfying tight shower shape requirements and at least 22 GeV.

IsoEle\_SH(1,30) represents one isolated electron candidate satisfying loose shower shape requirements and at least 30 GeV.

In the cases like CEM(2,3)CEM(1,9), the trigger bits are “AND’d” together, so in this instance, the event will pass the trigger if two trigger towers contain at least 3 GeV, and one of those contains at least 9 GeV. More information on triggers can be found in the trigger database [20].

## 4.2 Trigger Efficiencies

All of the events in this analysis are required to have fired an unprescaled trigger from its respective trigger version listed above. These triggers and their respective efficiencies, including their “OR’d” response, have been studied by the Electron ID group and used in other analyses at D0 [21, 22, 23], and only highlights will be presented here.

The trigger efficiencies were measured using a tag-and-probe method where  $Z \rightarrow e^+e^-$  events were used by requiring two electron candidates with an invariant mass  $> 65$  GeV, or near that of the Z boson [24]. One of the candidates becomes the “tag” and must pass tight electron identification cuts, while the other candidate, the “probe”, is used to measure the trigger efficiency. The “OR’d” response of these triggers was studied, and while flat in  $\eta_{det}$  and  $\phi_{det}$ , the response has a  $p_T$  dependence, often referred to as turn-on, and is shown in Figure 4.1. Their parameterizations can be found elsewhere [22].

Due to the changes in triggers and trigger list versions, an average trigger efficiency must be calculated. This efficiency is weighted by the percentage of total integrated luminosity collected by each trigger version and is shown in Table 4.2. The estimated trigger efficiency for the diphoton process is  $0.99 \pm 0.05$ .

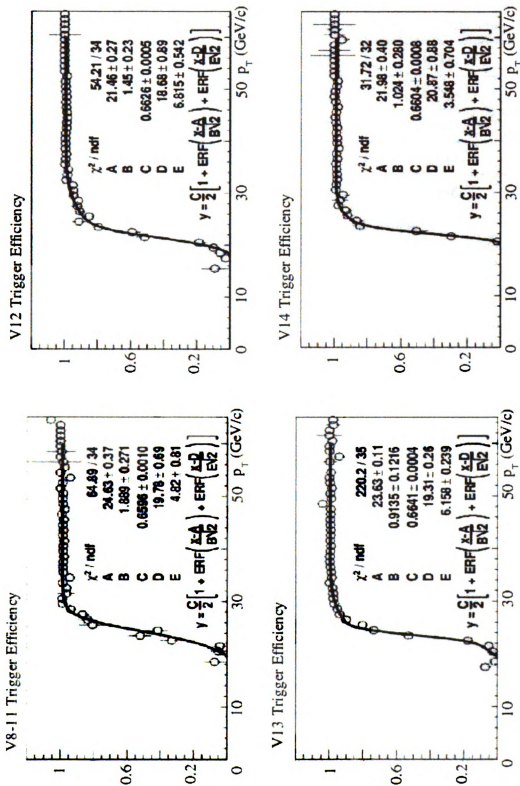


Figure 4.1. Trigger turn-on curves for OR'd single EM triggers [23].

Trigger Version	Efficiency	Trigger Lum.	Weighted Efficiency
v8-v11	0.975	0.102	0.099
v12	0.996	0.221	0.220
v13	0.984	0.359	0.353
v14	0.987	0.318	0.314
Total		1.0	0.986

Table 4.2: Summary of trigger efficiencies.

### 4.3 Dataset

The data used in this analysis were recorded between October 2002 and February 2006. These data were reconstructed using DORECO production release 17 (p17) and use trigger lists v8-v14. These data amount to a total integrated luminosity of  $1046.19 \text{ pb}^{-1} \pm 6\%$ , and are broken up by trigger version in Table 4.3.

Trigger List	$\int \mathcal{L}(\text{pb}^{-1})$
v8	5.81
v9	24.78
v10	10.75
v11	65.24
v12	230.96
v13	375.55
v14	333.11
Total	1046.19

Table 4.3: Total integrated luminosity by trigger list.

The datasets used here come from two different CSG skims. The first is the 2EMhighpt skim and is comprised of two data definitions. The first definition is `CSG_CAF_2EMhighpt_PASS3_p17.09.03`, and contains data from runs 165973-210437. The second definition is `CSG_CAF_2EMhighpt_PASS2_p17.09.01`, and contains data from runs 210442-215670. The two data definitions were broken up this way due to a mistake found in the hadronic calibration and fixed before processing runs 210442-215670. The 2EMhighpt skim requires two EM objects of  $|ID| = 10, 11$  and  $p_T > 12 \text{ GeV}$ . The second skim is the QCD skim and, for the same reason as above, also has two definitions which are `CSG_CAF_QCD_PASS3_p17.09.03`

and `CSG_CAF_QCD_PASS2_p17.09.01`. The QCD skim requires one of the following jet triggers to fire: `JT_125TT`, `JT_95TT`, `JT_65TT`, `CJT5`, `JT_8TT`, `JT_15TT`, `JT_25TT_NG`, `JT_45TT`, `JT_L3M225`, `JT_L3M250`, `JT_L3M380`, `JT_L3M430`. Both skims are further skimmed down using a copy of the `photon_id_tools` CAF package similar to [25] and stored into ROOT-tuples, a ROOT-based [26] data format.

### 4.3.1 Data Quality

Not all the data collected at D0 are used in this analysis. Some data are rendered useless due to issues like malfunctioning detectors or problems with electronics read-out. These problems are tracked and studied by the Data Quality group and released to the collaboration. The results are linked in CAF and remove runs of bad data and bad luminosity blocks.

A run of data is defined as the data recorded from when the DAQ software starts recording to when it stops. Every time the DAQ software is started and stopped, a unique run number is assigned to that run of data. If a detector subsystem shifter observes a malfunction during a particular run of data, they will mark that run as bad according to their detector sub-system. Also, if the Data Quality group finds a problem during offline examination, they will also mark it as bad. All of these are recorded in the bad runs list.

Sometimes small malfunctions occur during the course of a run that only require a small piece to be discarded. Since runs can sometimes last a few hours, it is better to discard only the problematic data rather than the entire run. This can be done by recording the luminosity block number (LBN) and marking it as bad. A luminosity block is the basic unit of time for a luminosity measurement. Each block has a unique number assigned to it and corresponds to a separate raw data file. These luminosity blocks are incremented for every start of data recording, every initialization of the trigger framework, or every 60 seconds [11]. If a problem occurs, these LBNs can be

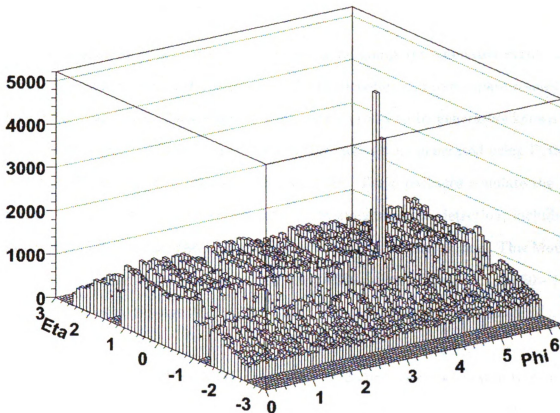


Figure 4.2. Eta vs. Phi lego plot illustrating hot cells.

vetoed without biasing the luminosity calculation. These bad LBNs are tabulated by the Data Quality group.

Certain run numbers were noted to contain an excess of events with two EM candidates that continually occur at the same location in eta-phi space, as can be seen in Figure 4.2. Due to the extremely low probability of this occurring naturally, these runs are believed to contain hot cells in the calorimeter, and, consequently, were manually discarded from this analysis and accounted for in the luminosity calculation.

## 4.4 Monte Carlo

While this analysis is primarily data driven, some computer simulated events are used as a means to predict the response of the D0 detector and to compare results to theoretical predictions. These simulated events are produced by generators known as Monte Carlo. The diphoton samples used in this analysis are generated using Pythia 6.3 [27], CTEQ6L1 PDF's [28], and GEANT3 [29]. These packages simulate the  $p\bar{p}$  interaction from collision and hard scatter to fragmentation to detection, including effects of the D0 detector materials and magnetic field, to reconstruction. This Monte Carlo was produced in three mass ranges with 98250 events of range  $M_{\gamma\gamma} = 50 - 130$  GeV, 51500 events of range  $M_{\gamma\gamma} = 130 - 250$  GeV, and 26750 events of range  $M_{\gamma\gamma} = 250 - 500$  GeV.

RESBOS [30] and DIPHOX [31] theoretical predictions are also used in this analysis. The RESBOS prediction comes from [32], and is a theoretical prediction that includes all-orders soft-gluon resummation and is valid to next-to-next-to-leading logarithmic accuracy. The DIPHOX Monte Carlo, [33], is an event generator at the parton level designed to calculate the hadroproduction of two photons. It provides a prediction up to NLO, but does not include gluon box contributions at NLO. Since the DIPHOX prediction does not include gluon box diagram components at NLO, and will be added from another source, the LO gluon box component was removed from the DIPHOX calculation. Both the LO and NLO were then calculated from [34] and added into the DIPHOX prediction. Since there are inherent differences in these theory calculations, some differences are expected between the predictions.

# CHAPTER 5

## Photon ID and Background Study

This chapter will discuss the variables and search techniques for identifying photons in a hadron collider. It will describe the reconstruction algorithms that RECO uses to identify photon-like objects and the analysis cuts used to fully identify photons. The sources of background and specifically how the analysis cuts reject much of this background and the associated cut efficiencies will also be presented here.

### 5.1 Reconstruction Algorithms

As previously stated in Section 3.11, after an event passes the different trigger levels, it is written to tape. Then, offline, the D0RECO software, using various algorithms, reconstructs all of the particles detected in the event and stores them in a TMB. Photons and electrons (electrons are taken to mean both electrons and positrons) are reconstructed as follows: A group of calorimeter towers in a cone of  $R = 0.4$ , where

$$R = \sqrt{\Delta\eta^2 + \Delta\phi^2} \quad (5.1)$$

centered around a calorimeter tower of high energy content is identified as an EM cluster. This cluster must have a minimum transverse energy of 1.5 GeV, and an electromagnetic fraction, as defined in Section 5.2, of  $EMF > 0.9$ . If a track exists

within

$$|\eta_{cluster} - \eta_{track}| < 0.05 \text{ and } |\phi_{cluster} - \phi_{track}| < 0.05$$

this cluster will be assigned  $|ID| = 11$ , and if not, the cluster will be assigned  $ID = 10$ . An EM cluster with  $|ID| = 10$  or  $11$  is considered a loose EM candidate, or a potential photon or electron. The D0RECO software also accounts for a number of other corrections due to geometrical effects, non-linearities in electronics, hot cells, and calorimeter noise [37, 38].

## 5.2 Particle Signatures

There are many particles that can be produced in proton+anti-proton collisions. In order to distinguish between these different particles, it is important to know what characteristics each one has so that one can distinguish between them.

### 5.2.1 Photons

A photon (or gamma particle) is simply a particle of light. It is massless, chargeless, and is entirely electromagnetic in nature. As a result, one can exploit these characteristics to distinguish photons from other particles.

When a photon travels through the D0 detector, it leaves a signature of:

- a narrow electromagnetic shower in the calorimeter
- no tracks matched to the electromagnetic shower

### 5.2.2 Electrons

Electrons are particles that are also electromagnetic in nature. As such, electron signatures are very similar to those of photons. Electrons have a key difference,

however, in that they carry an electric charge that will not only cause a deflected trajectory in the magnetic field of the detector, but also leave a matched track in the detector.

### 5.2.3 Jets

A jet is a relatively localized spray of particles that can consist of both electromagnetic and hadronic particles. Because jets contain many particles, the showers that develop in the calorimeter are often much wider than those of electrons and photons, the showers often develop much deeper in the detector into the hadronic sections, which does not happen with electrons and photons, and the particles can leave many associated tracks.

### 5.2.4 Muons

Muons are particles that typically pass through the calorimeter without depositing any significant amount of energy. These particles are, however, detected in the muon system described in Section 3.8. Since this analysis is not concerned with muons, further detail will not be given here.

## 5.3 Signal Variables

Due to these characteristics of photons, electrons, and jets, some variables are defined to better distinguish these particles: electromagnetic fraction, isolation, track probability, track isolation, and missing  $E_T$ .

Electromagnetic fraction (EMF) is defined as

$$EMF = \frac{E_{EM}}{E_{total}} \quad (5.2)$$

where  $E_{EM}$  is the energy deposited in the electromagnetic layers of the calorimeter, as described in Section 3.7, and  $E_{total}$  is the total energy deposited in the the calorimeter. A high EMF (value  $> 0.9$ ) corresponds to an object that deposits most of its energy in the EM layers of the calorimeter, such as a photon or an electron.

Isolation (iso) is defined as

$$iso = \frac{E_{total}(R < 0.4) - E_{EM}(R < 0.2)}{E_{EM}(R < 0.2)} \quad (5.3)$$

where  $E_{total}(R < 0.4)$  is the total energy deposited in the calorimeter in a cone of radius 0.4 and  $E_{EM}(R < 0.2)$  is the energy deposited in the EM portion of the calorimeter in a cone of radius 0.2. Iso is a measure of how isolated an electromagnetic object is in the calorimeter. A small isolation (iso  $< 0.2$ ) corresponds to a single electromagnetic object where no other particles traveled through the detector close-by. If another particle were to travel through the detector nearby (within  $\Delta R < 0.4$ ), it would cause a larger value.

Track matches are done using a probability. First, the tracks are reconstructed by extrapolating them from their origin to the EM3 layer (the most segmented calorimeter layer). Next, the position of the EM object and the track are compared using the equation

$$\chi^2 = \left(\frac{\delta\eta}{\sigma_\eta}\right)^2 + \left(\frac{\delta\phi}{\sigma_\phi}\right)^2 \quad (5.4)$$

where  $\delta\eta$  is the difference in  $\eta$  between the track and the EM object,  $\delta\phi$  is the difference in  $\phi$  between the track and the EM object, and  $\sigma_\eta$  and  $\sigma_\phi$  are the root-mean-square (RMS) values of  $\eta$  and  $\phi$ , respectively, determined by experimental distributions [36]. A spatial track match of  $\chi^2 > 0.01$  is considered to be a track match with a 77% efficiency [36].

Track isolation (IsoHC4) is defined as the  $p_T$  sum of all tracks within a hollow

cone. This hollow cone is of size  $0.05 < \Delta R < 0.4$ , and the sum must be below 2 GeV/c. This variable is used to remove particles that have any kind of activity in the tracking portion of the detector, since photons' signatures do not contain a track.

Missing transverse energy,  $\cancel{E}_T$ , as described in Section 3.4, is found by performing a total energy conservation in the transverse plane, and returning a non-zero value.  $\cancel{E}_T$  is produced when either energy is added to the event by an outside source, or, the more likely instance, by undetected particles such as neutrinos, which cannot be directly detected with the D0 detector. Cosmic rays are continually bombarding the earth and the D0 detector, and while the odds are quite small, it is possible for a cosmic ray to be detected in the calorimeter and leaving a photon-like signature. As such, a cut of  $\cancel{E}_T < 30$  GeV is employed as a precautionary measure, and removes only 2.5% of the events.

Some distributions of these variables in the dataset are shown in Figure 5.1.

## 5.4 Background

A number of event topologies do exist that contain objects whose signature resembles that of a photon. These topologies are referred to as background, and need to be minimized as much as possible. The main source of background is a jet that leaves a signature that is similar to a photon, called a fake-photon. This can occur, for example, if the jet contains a neutral pion ( $\pi^0$  or pizero) that carries most of the jet's associated momentum. Pizeros typically decay to two photons (more than 98% of the time [35]), and due to the pizero being energetic and of low mass ( $134.97\text{MeV}/c^2$  [35]), the opening angle between the two photons is very small. This angle is so small, in fact, that the two photons can appear as one in the detector. They can, however, have a wider shower shape in the detector than the average photon, and the probability of one of these two photons beginning its shower in the preshower

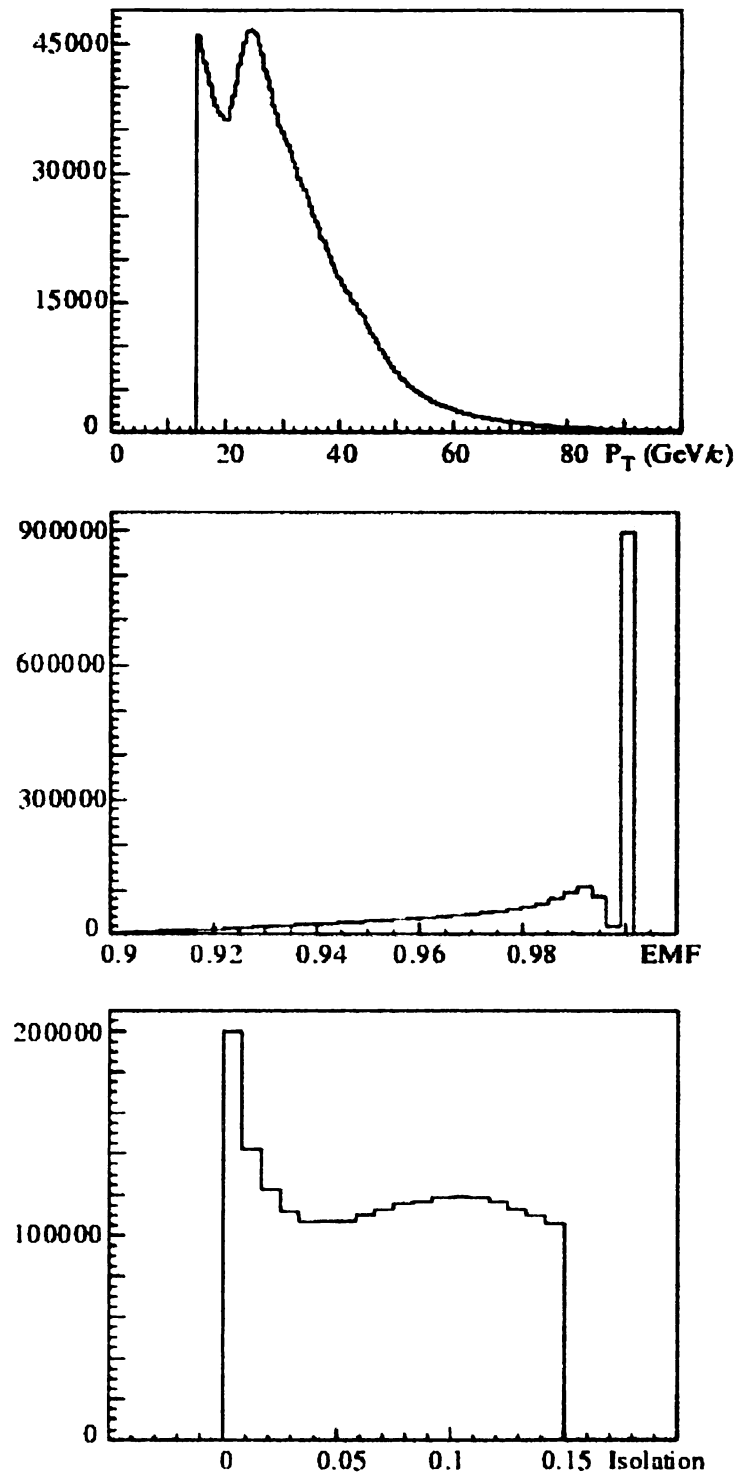


Figure 5.1. Distributions of signal variables  $P_T$  (top), EMF (middle), and iso (bottom).

detectors is enhanced compared with a single photon.

While these features can also be exploited to remove some of these events, some will still remain as irreducible background. At that point, all that can be done is to statistically estimate how much of this background is present in the overall measurement.

## 5.5 Analysis Cuts and Efficiencies

### 5.5.1 Analysis Cuts

As this analysis is concerned with measuring the diphoton cross-section, background suppression is a key component to an accurate measurement. As such, some tight cuts are applied to the above variables that will appropriately remove much of the QCD fake-photon contribution. The cuts used here are  $EMF > 0.95$ ,  $iso < 0.07$ ,  $trkprb < 0.001$ ,  $IsoHC4 < 2.0$  GeV/c, and  $\cancel{E}_T < 30$  GeV. Some of the distributions relating to the cuts are shown in Figure 5.2. In addition to these cuts, a couple of geometric cuts are also applied.

The D0 detector phi-cracks as mentioned in Section 3.7, require some careful analysis. In order to minimize the effect of these cracks in particle measurements, a cut is employed, referred to as a phi-fiducial cut, to remove events that have particles near these cracks. This phi-fiducial cut is not well-modeled in the MC, and cuts out approximately 9% more events than it should. This discrepancy is accounted for when determining the analysis cut efficiencies, and is shown in Figure 5.3. The average acceptance in the MC is 70.81%, while the average acceptance in the data is 77.78%.

Also, the detector, as pictured in Figure 3.11, has large gaps between the central calorimeter and the end-caps. These inter-cryostat detector (ICD) regions are

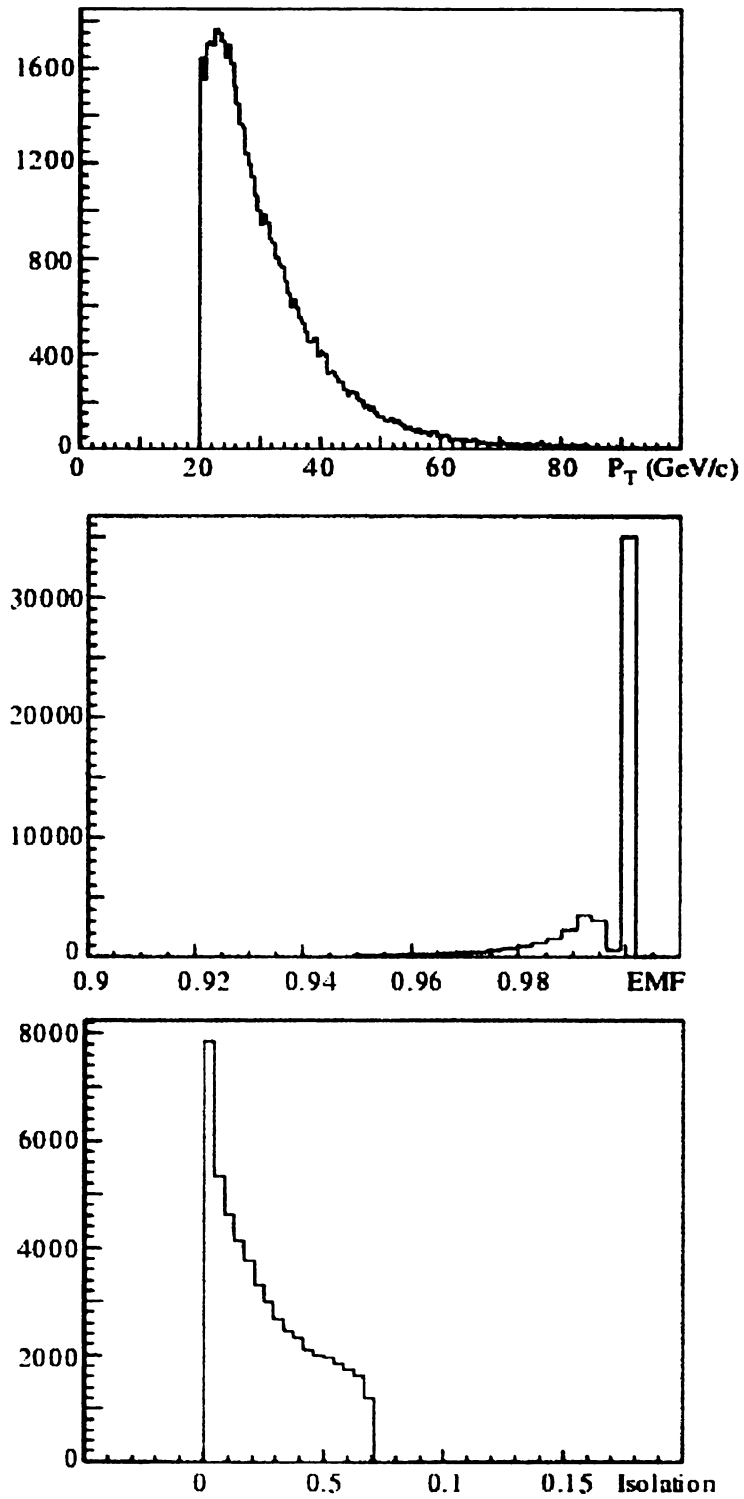
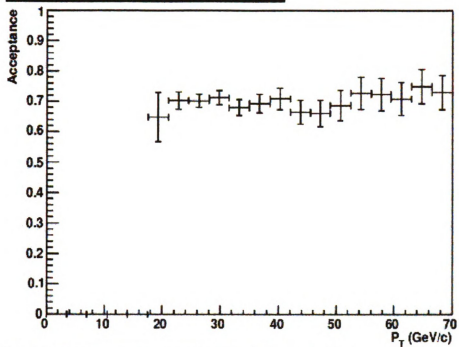


Figure 5.2. Distributions of the analysis cuts  $P_T$  (top), EMF (middle), and iso (bottom).

**diphotonMC Phi\_Fidu Acceptance**



**2EMhighptdata Percent Phi\_Fidu Accepted**

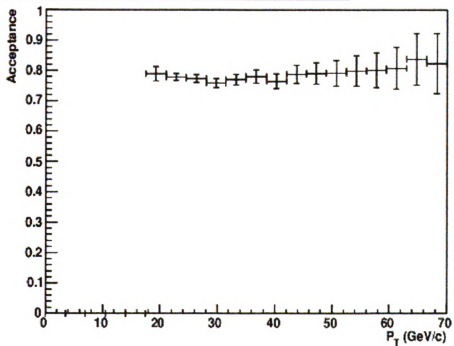


Figure 5.3. Phi\_fiducial acceptances as a function of  $p_T$  in diphoton MC (top) and data (bottom).

problematic and are not well-understood. In addition, the tracking efficiency in the end-caps is slightly worse than in the central calorimeter, as well as the complimentary algorithms for the preshower detectors of the CC are not available in the EC. Thus, a pseudorapidity cut of  $|\eta_{det}| < 1.1$  is applied to the data to remove these concerns.

Finally, the  $p_T$  threshold is raised on the highest energy photon to 21 GeV while the threshold on the second highest energy photon is set at 20 GeV. These  $p_T$  cuts were selected to improve the trigger efficiency as well as to properly compare our result to theories that prefer asymmetric transverse momentum cuts.

The distribution of di-EM events as a function of mass prior to these cuts is shown in Figure 5.4.

Note the presence of a peak due to the process  $Z \rightarrow e^+e^-$ . The result of these cuts on the dataset is presented in Figure 5.5 as a function of mass.

### 5.5.2 Cut Efficiencies

The efficiencies of the above cuts have been measured using a diphoton MC as described in Section 4.4, and have distributions presented in Figures 5.6 and 5.7.

The efficiencies are defined as

$$\varepsilon = \frac{N_{tight}}{N_{MC}} \quad (5.5)$$

where  $\varepsilon$  is the efficiency,  $N_{tight}$  is the number of events satisfying the tight analysis cuts, and  $N_{MC}$  is the number of input Monte Carlo events. The efficiencies are measured on a bin-by-bin basis and as a function of Mass,  $q_T$ , and  $\Delta\phi_{\gamma\gamma}$ . These efficiencies are then used on a bin-by-bin basis and are presented in Figure 5.8. For masses below  $50 \text{ GeV}/c^2$ , the efficiency is extrapolated.

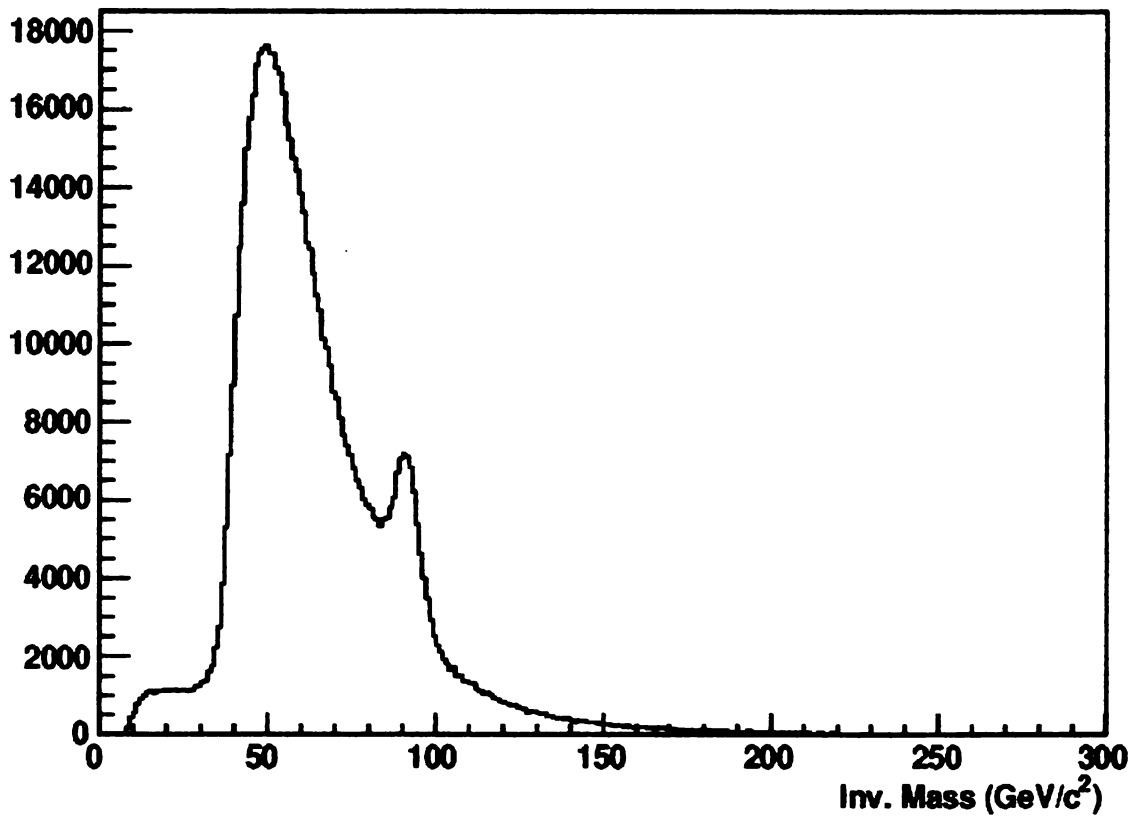


Figure 5.4. Di-EM Mass Spectrum.

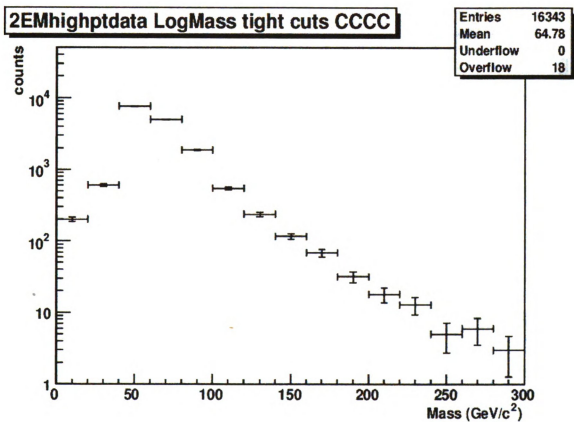


Figure 5.5. Di-EM Mass Spectrum after analysis cuts.

## 2EMhighptdata Mass tight cuts CCCC

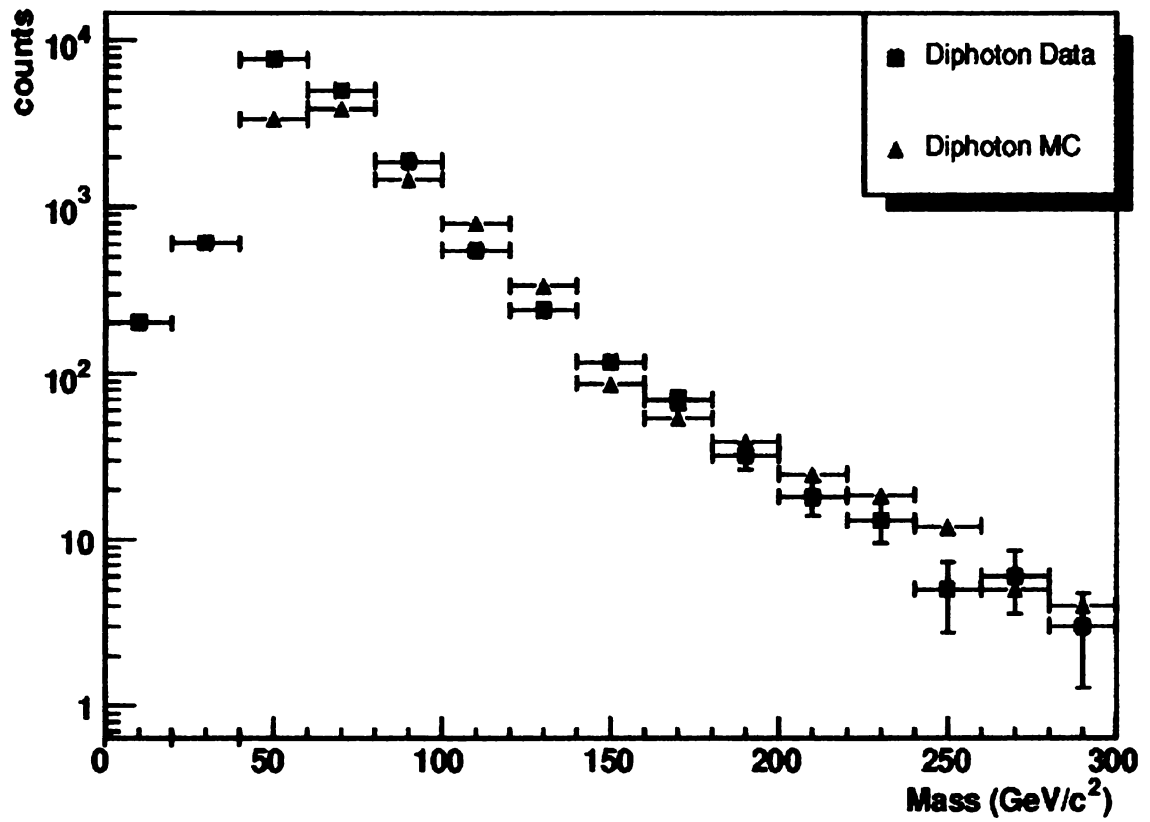


Figure 5.6. Distribution of diphoton Monte Carlo overlaid with data.

### DiphotonMC Single Photon Pt

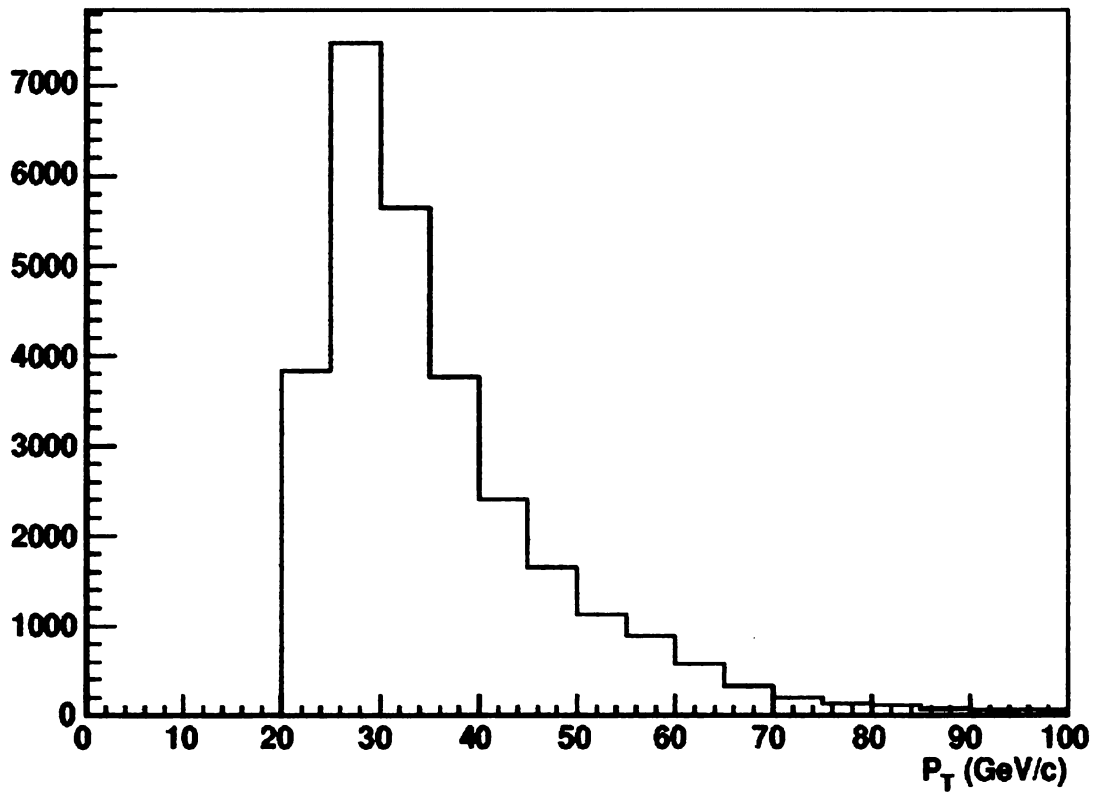


Figure 5.7.  $p_T$  distribution of single photons from diphoton Monte Carlo.

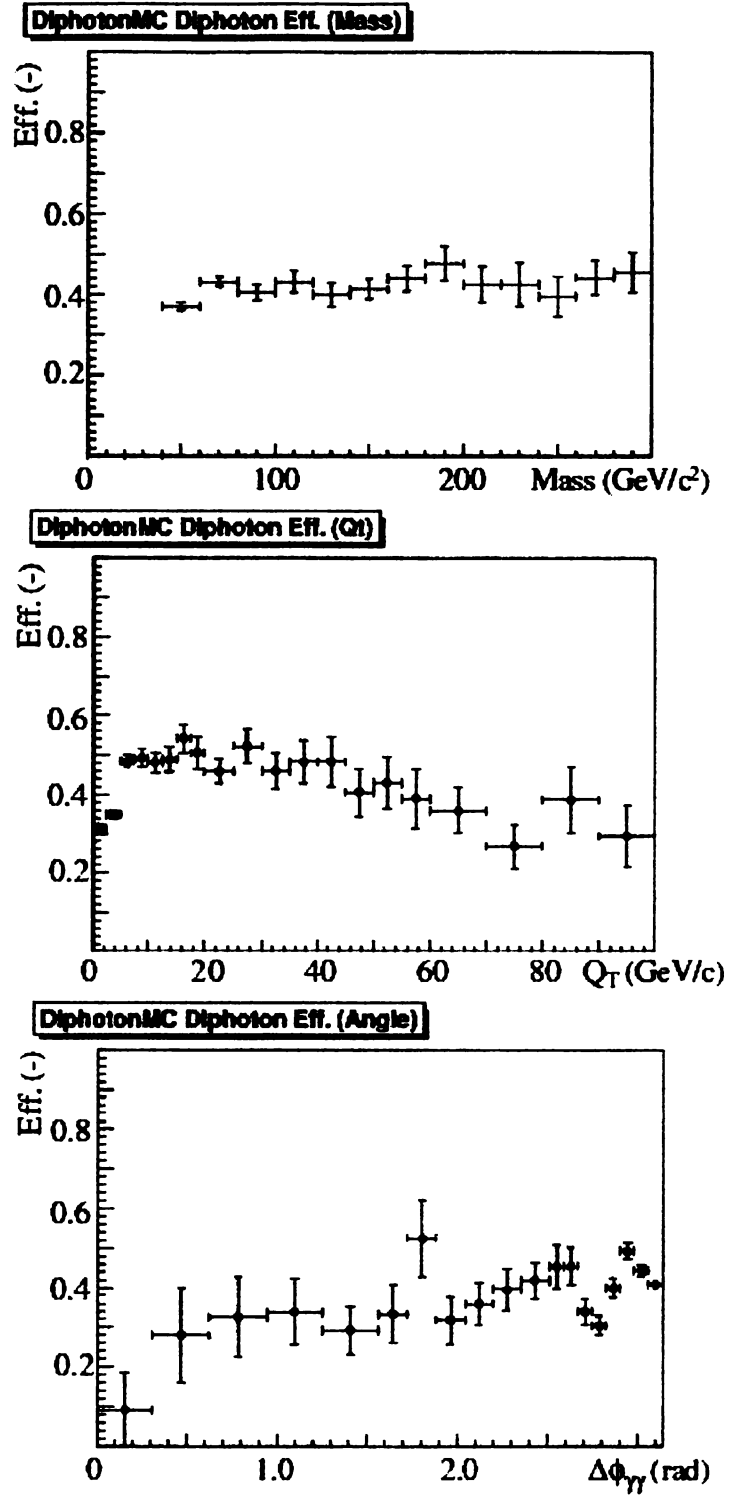


Figure 5.8. Analysis Cut Efficiencies as a function of Mass (top),  $q_T$  (middle), and  $\Delta\phi_{\gamma\gamma}$  (bottom).

## Data Smearing

The calorimeter has a particular energy resolution that can cause energy measurements to be slightly above or below the actual value, an effect known as smearing. Due to the relative shape of these histograms, this smearing can cause an excess of events in the neighboring histogram bin. This smearing has been modeled in the computer simulated detector, and is accounted for in these efficiencies, as the  $N_{tight}$  is considered to be a detector smeared value, and the  $N_{MC}$  is an unsmeared input value. The application of the efficiencies in Figure 5.8 will effectively unsmear the data and yield the true cross-section measurement.

The efficiencies shown here shall be applied to the data in the following chapter.

# CHAPTER 6

## Cross-Section Analysis

This chapter will explain the method used to separate the diphoton signal from background events, thus yielding a final cross-section. The variables used will be described, the mathematics involved will be explained, and the final cross-section measurement including efficiencies and associated errors will be presented.

### 6.1 Matrix Inversion Method

As mentioned in Section 5.4, even though the analysis cuts have exploited the difference in particle signatures in the detector to remove events that do not contain diphotons, some background events remain. Now, a statistical method must be employed to separate the portion of true gamma-gamma events from gamma-jet and jet-jet events where the jets have signatures similar to that of a photon.

This statistical method requires a discrimination variable, a variable that shows a different response to photons and jets. When a cut is then placed on this variable, there will be efficiencies,  $\varepsilon_\gamma$ , for a photon to pass this cut,  $(1 - \varepsilon_\gamma)$ , for a photon to fail this cut,  $\varepsilon_j$ , for a photon-like jet to pass this cut, and  $(1 - \varepsilon_j)$ , for a photon-like jet to fail this cut. Given that the events in this analysis contain two photonic objects,

combinatorics suggests the following three equations:

$$N_{PP} = \varepsilon_\gamma^2 N_{\gamma\gamma} + \varepsilon_\gamma \varepsilon_j N_{\gamma j} + \varepsilon_j^2 N_{jj} \quad (6.1)$$

$$N_{PF} = 2\varepsilon_\gamma(1 - \varepsilon_\gamma)N_{\gamma\gamma} + [\varepsilon_\gamma(1 - \varepsilon_j) + (1 - \varepsilon_\gamma)\varepsilon_j]N_{\gamma j} + 2\varepsilon_j(1 - \varepsilon_j)N_{jj} \quad (6.2)$$

$$N_{FF} = (1 - \varepsilon_\gamma)^2 N_{\gamma\gamma} + (1 - \varepsilon_\gamma)(1 - \varepsilon_j)N_{\gamma j} + (1 - \varepsilon_j)^2 N_{jj} \quad (6.3)$$

where  $N_{PP}$  is the number of events where both objects pass the cut,  $N_{PF}$  is the number of events where one object passes and one object fails the cut,  $N_{FF}$  is the number of events where both objects fail the cut,  $N_{\gamma\gamma}$  is the number of events that contain a diphoton,  $N_{\gamma j}$  is the number of events that contain a photon + jet, and  $N_{jj}$  is the number of events that contain a jet + jet. Taking the coefficients of equations 6.1, 6.2, and 6.3, a matrix equation can be formed

$$\begin{pmatrix} N_{PP} \\ N_{PF} \\ N_{FF} \end{pmatrix} = \begin{pmatrix} \varepsilon_\gamma^2 & \varepsilon_\gamma \varepsilon_j & \varepsilon_j^2 \\ 2\varepsilon_\gamma(1 - \varepsilon_\gamma) & \varepsilon_\gamma(1 - \varepsilon_j) + (1 - \varepsilon_\gamma)\varepsilon_j & 2\varepsilon_j(1 - \varepsilon_j) \\ (1 - \varepsilon_\gamma)^2 & (1 - \varepsilon_\gamma)(1 - \varepsilon_j) & (1 - \varepsilon_j)^2 \end{pmatrix} \begin{pmatrix} N_{\gamma\gamma} \\ N_{\gamma j} \\ N_{jj} \end{pmatrix} \quad (6.4)$$

When the 3x3 matrix is inverted,  $N_{\gamma\gamma}$ ,  $N_{\gamma j}$ , and  $N_{jj}$  are determined, thus yielding the true diphoton signal.

## 6.2 Efficiency Data Samples

A pure set of photons should be examined using a discrimination variable, but no currently discovered particle of reasonably high energy and relatively high production

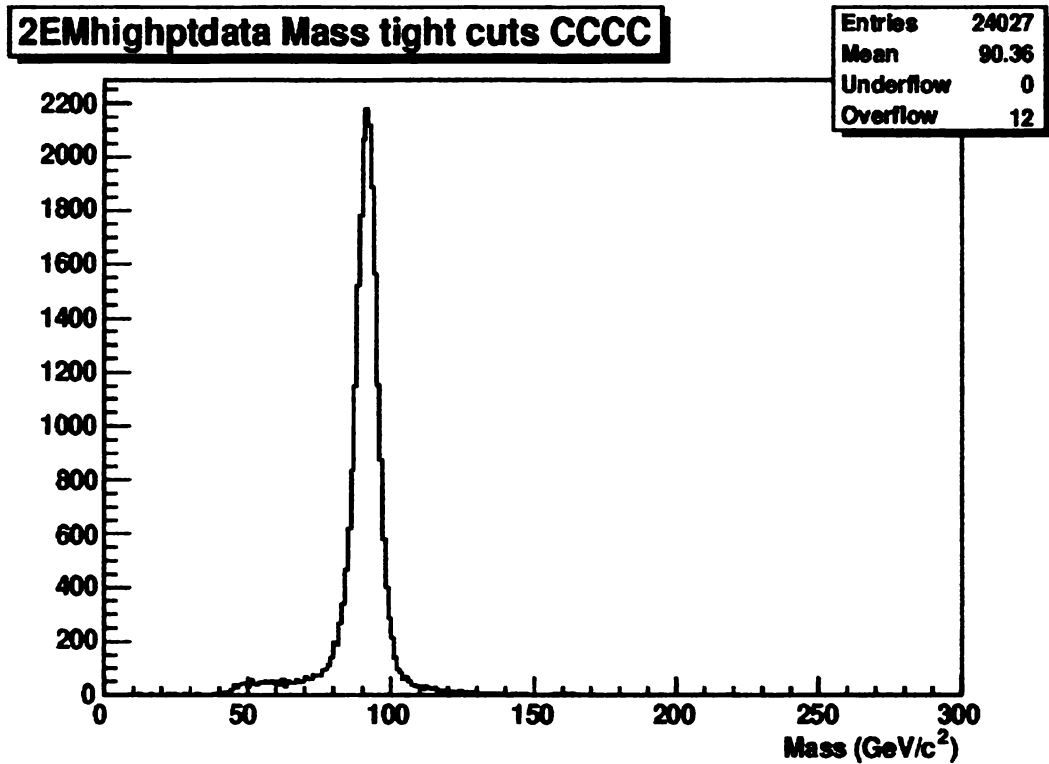


Figure 6.1. Histogram of the Z-mass from the data.

decays into photons, preventing the use of photons from data to tune the discrimination variable cut. Electrons, however, basically shower identically to photons in the detector, save for a matched track, and are often produced by a decaying Z boson. Since the Z boson has a well-known mass, a relatively high production rate, and decays into high energy electrons, it is possible to get a pure sample of electrons that will model a photon's response in the detector by selecting events in data that contain two electrons and possess a reconstructed invariant mass within the Z boson mass window. The Z-mass peak is presented in Figure 6.1.

Pure photon Monte Carlo samples could be used in lieu of this electron substitution, however, there are some observable differences between Monte Carlo and data that will be avoided by keeping this analysis data driven.

A pure set of photon-like jets in data is a little easier to obtain. The QCD dataset

detailed in section 4.3 is used, requiring in the event one good jet, an EM-object that passes the analysis cuts from section 5.5.1, and  $\cancel{E}_T < 10$  GeV to remove event topologies such as  $W \rightarrow e\nu$  that would naturally contain a jet and an electron and bias the efficiency. A good jet is defined in [39].

The efficiencies of the electrons or photon-like jets to pass the discrimination cut are measured as a function of  $p_T$ , and are determined by

$$\varepsilon_{\gamma/j} = \frac{N_{Pass}}{N_{Pass} + N_{Fail}} \quad (6.5)$$

## 6.3 Discrimination Variables

Presented in the following subsections are three variables that do show a difference between photons and jets and will be used as the discrimination variables in this analysis.

### 6.3.1 Phi Width

Phi Width is a measure of the width squared of the object's shower measured by the EM3 layer of the calorimeter. The larger the value, the wider the shower the object created in the calorimeter. Histograms of the phi width of photons in MC, electrons in data, and EM-jets in data are shown in Figure 6.2, and show that large values correspond to jets, while smaller values correspond to electrons and photons. In agreement with the D0 Photon-ID group, a cut is placed at  $Phi\ Width < 14\ cm^2$  [40]. The related efficiencies of this cut are shown in Figure 6.3 as a function of  $p_T$ .

### 6.3.2 CPS\_RMS

The CPS\_RMS variable is an energy weighted root-mean-square of the difference in each strip's phi position with that of the EM3 layer's phi position. This is done for

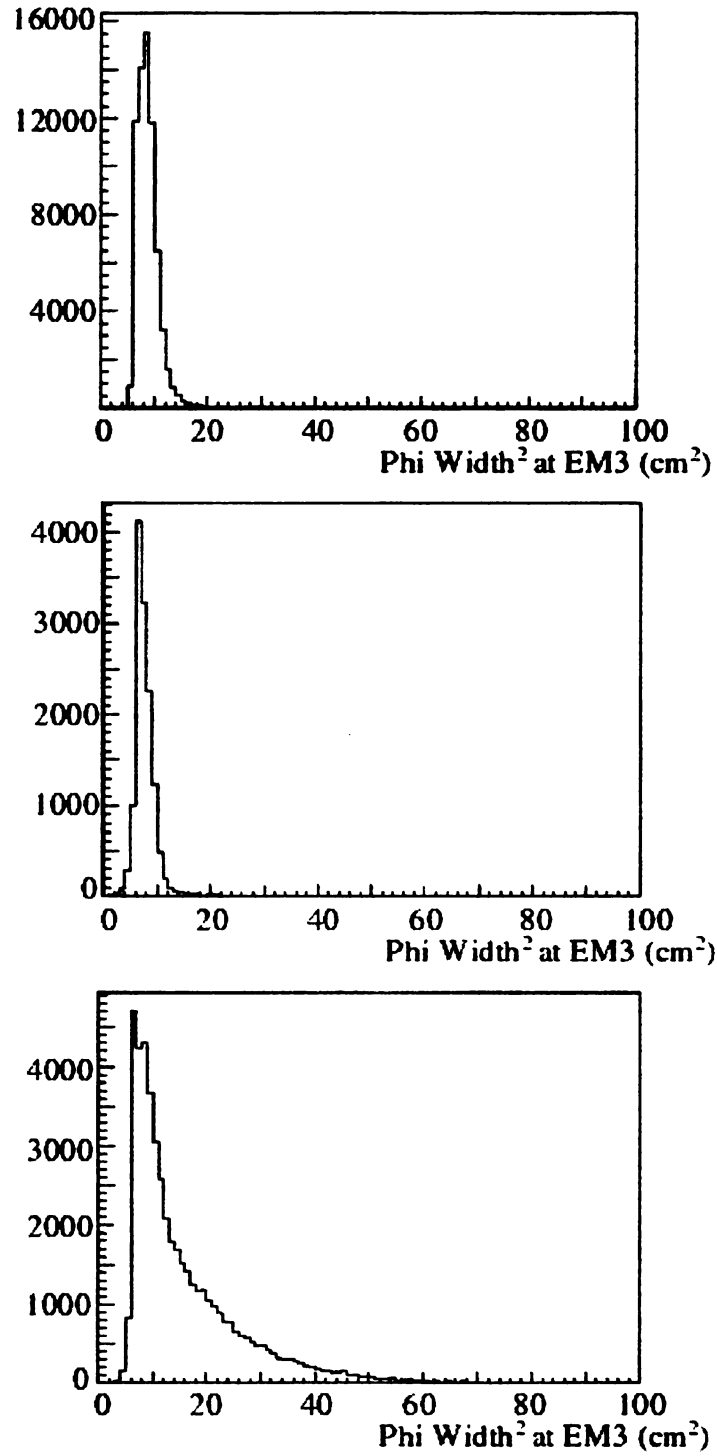
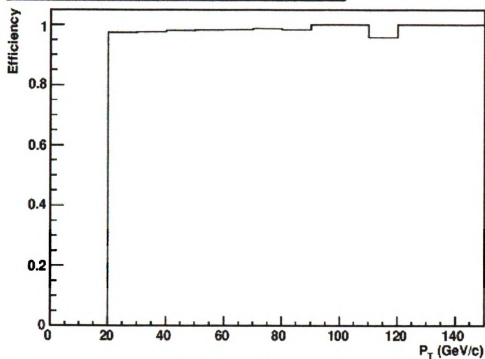


Figure 6.2. Distributions of the Phi Width variable in electrons (top), MC photons (middle), and jets (bottom).

**2EMhighptdata Eff. Phi Width(Pt) in CC**



**QCDdata Eff. Phi Width(Pt) in CC**

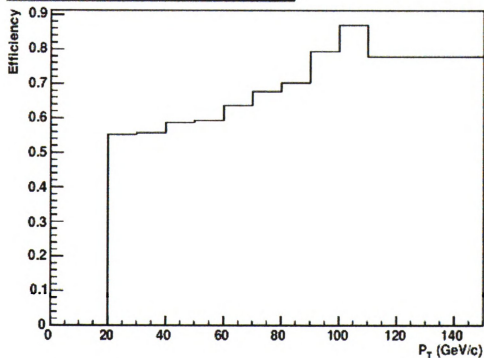


Figure 6.3. Efficiencies of electrons (top) and jets (bottom) of the Phi Width discrimination variable as a function of  $p_T$ .

every strip in a CPS cluster and the result is the sum of each layer. Large values correspond to particles with large widths in the CPS detector, such as jets, whereas small values correspond to particles such as photons and electrons. Distributions of this variable for photons in MC, electrons in data, and jets in data are shown in Figure 6.4. A cut is placed at  $\text{CPS\_RMS} < 0.003$ , and the efficiencies for this cut are shown in Figure 6.5 as a function of  $p_T$ . More information on how this variable is determined can be found in [41].

### 6.3.3 CPS\_RMS Squared

The  $\text{CPS\_RMSSQ}$  variable is similar to the  $\text{CPS\_RMS}$  variable except that the weighting is done by the energy of the strip squared. This is done in an effort to magnify the result when two objects pass through the CPS with a very small opening angle between them, such as a pizero that has decayed to two photons. Again, small values correspond to electrons and photons, whereas large values correspond to jets. This can be seen in the distributions presented in Figure 6.6.

A cut on this variable is placed at  $\text{CPS\_RMSSQ} < 0.0012$ , and the resulting efficiencies are shown in Figure 6.7 as a function of  $p_T$ .

More information on how this variable is calculated can also be found in [41].

## 6.4 Result of Matrix Inversion

Using the efficiencies in the plots presented, a matrix is produced and inverted for each  $p_T$  bin. The result for each discrimination variable is determined independently, overlaid on each other, and shown in Figures 6.8, 6.9, and 6.10.

The matrix inversion is applied to the mass distribution on a bin-by-bin basis

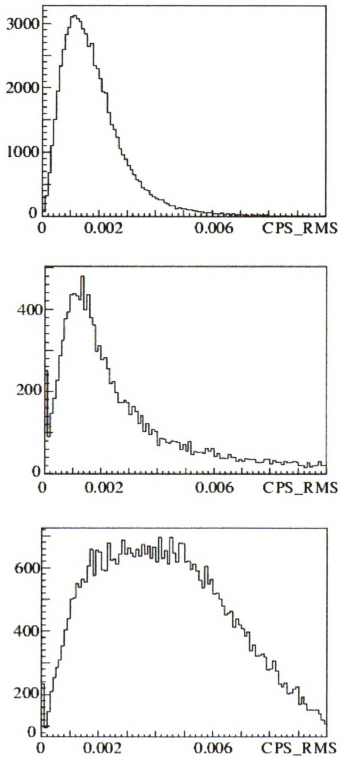
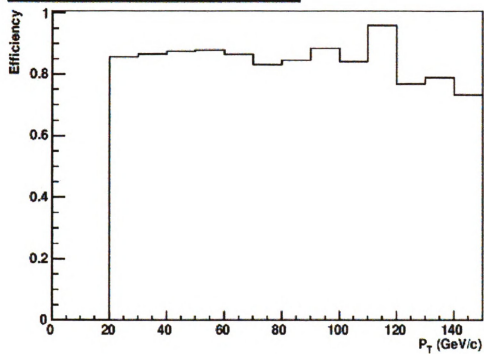


Figure 6.4. Distributions of the CPS\_RMS variable in electrons (top), MC photons (middle), and jets (bottom).

**2EMhighptdata Eff. CPS(Pt) in CC**



**QCDData Eff. CPS(Pt) in CC**

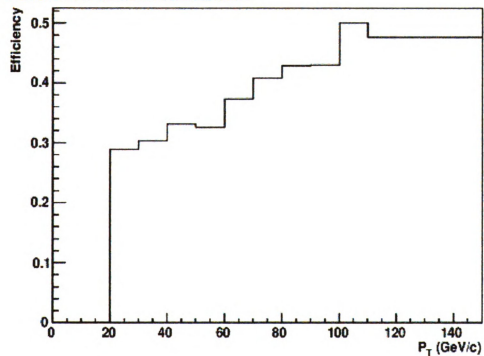


Figure 6.5. Efficiencies of electrons (top) and jets (bottom) of the CPS\_RMS discrimination variable as a function of  $p_T$ .

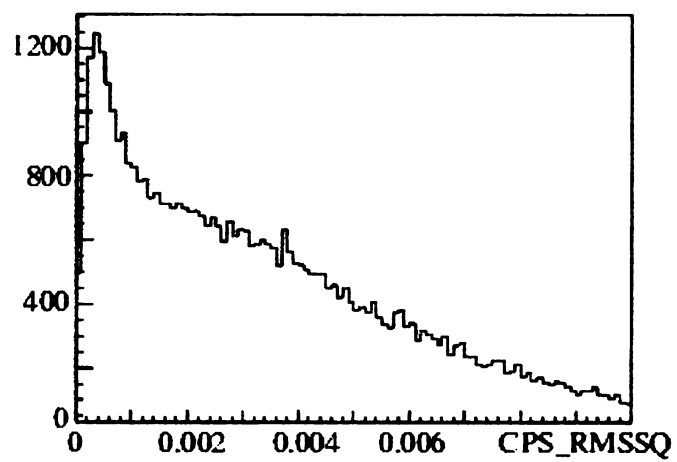
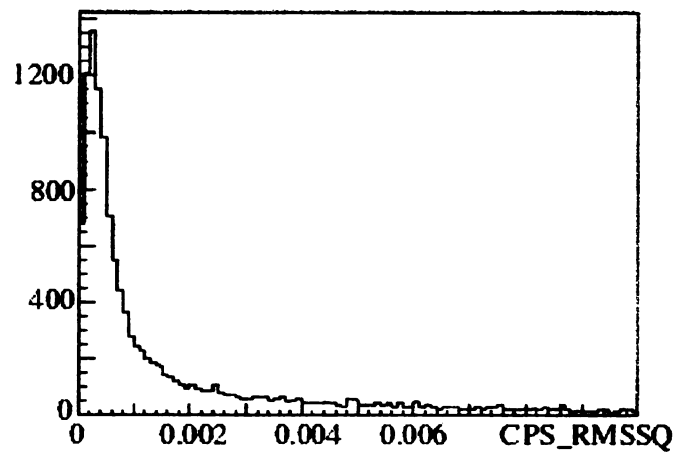
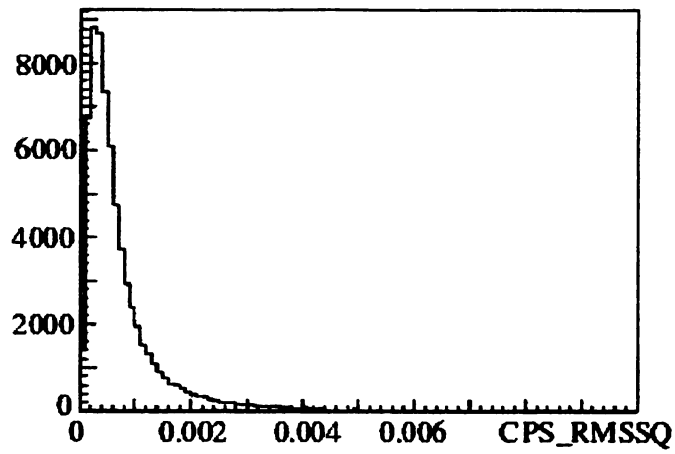
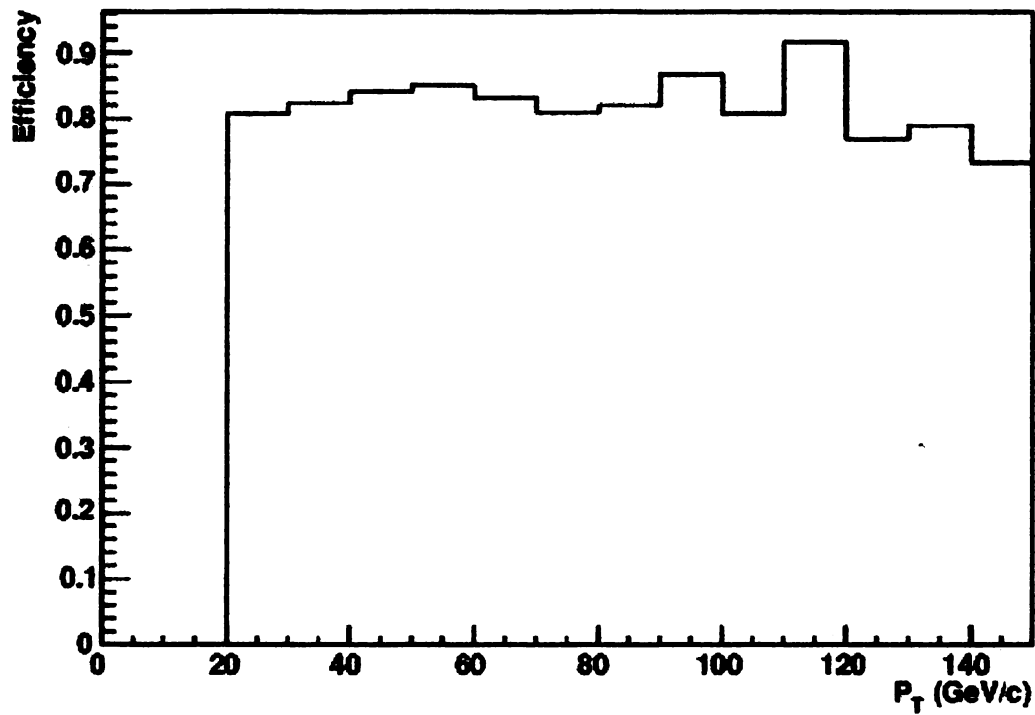


Figure 6.6. Distributions of the CPS\_RMSSQ variable in electrons (top), MC photons (middle), and jets (bottom).

**2EMhighptdata Eff. CPS\_SQ( $p_T$ ) in CC**



**QCDdata Eff. CPS\_SQ( $p_T$ ) in CC**

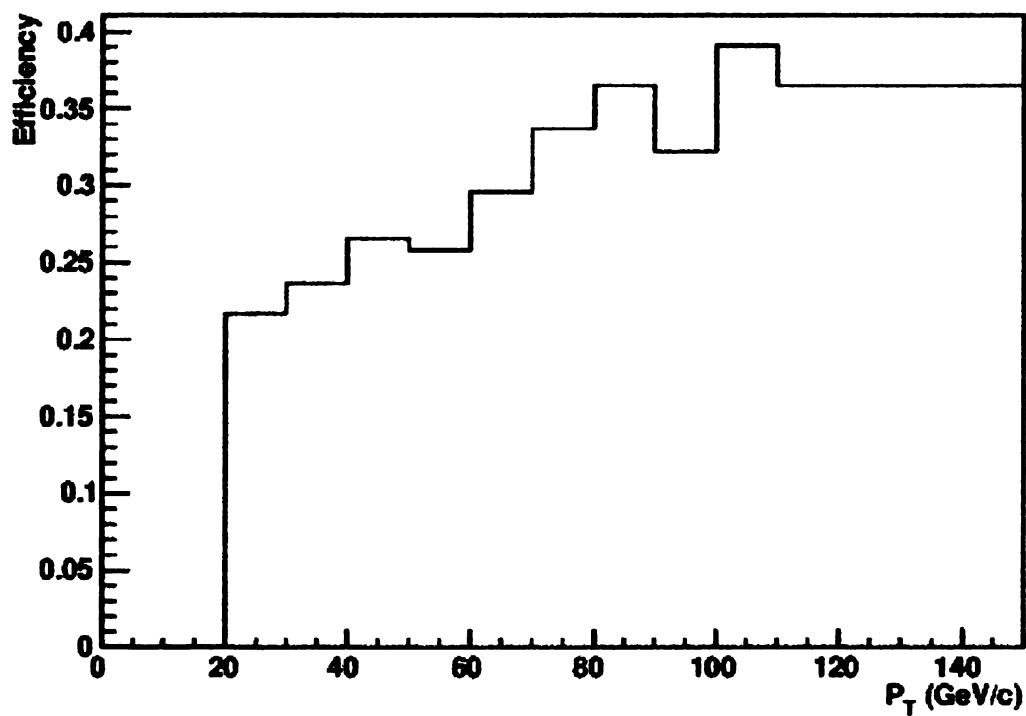


Figure 6.7. Efficiencies of electrons (top) and jets (bottom) of the CPS\_RMSSQ discrimination variable as a function of  $p_T$ .

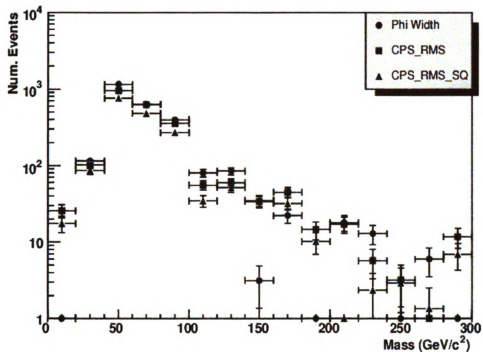


Figure 6.8. Diphoton events determined by matrix inversion of discrimination variable efficiencies as a function of mass.

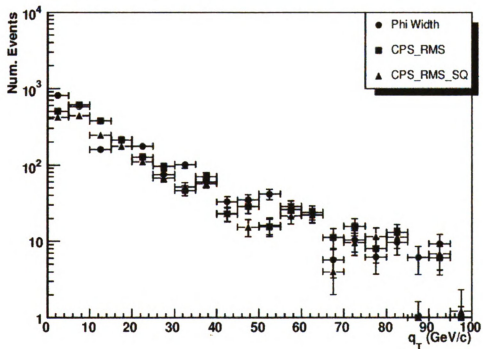


Figure 6.9. Diphoton events determined by matrix inversion of discrimination variable efficiencies as a function of transverse momentum.

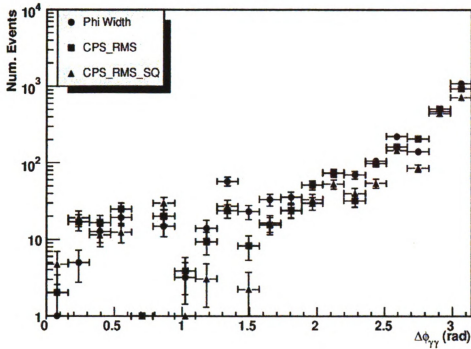


Figure 6.10. Diphoton events determined by matrix inversion of discrimination variable efficiencies as a function of opening angle between the two photons.

using the good approximation that

$$p_T^\gamma \approx \frac{M_{\gamma\gamma}}{2} \quad (6.6)$$

For the distributions of transverse momentum of the diphoton and the opening angle between the two photons, an average efficiency across all  $p_T$  is used for the matrix inversion. These distributions show good agreement, and will provide a method of determining the systematic errors involved with this matrix inversion method.

## 6.5 Cross-Section

Given the equation,

$$N_{\gamma\gamma} = \sigma_{\gamma\gamma} \mathcal{L} \quad (6.7)$$

where  $N_{\gamma\gamma}$  is the number of direct diphoton events found in a dataset containing luminosity,  $\mathcal{L}$ , the cross-section of the direct diphoton process,  $\sigma_{\gamma\gamma}$ , can now be calculated. The cross-section is calculated as a function of mass,  $q_T$ , and opening angle by averaging the three separate results of the matrix inversion, dividing by the luminosity from Section 4.3, and applying the efficiencies from the previous sections. Application of the efficiencies will account for true diphoton events removed by the analysis cuts, thus correcting  $N_{\gamma\gamma}$  to its true value. Figures 6.11, 6.12, and 6.13 show the differential cross-section for direct diphoton production as a function of invariant mass of the diphoton, the  $q_T$  of the diphoton, and the opening angle between the two photons, respectively.

The dotted line at the bottom of each plot is a nominal line, while the solid curve around it expresses the systematic error on the data. The systematic errors on the mass plot range from 4.9% at the mass peak to 160% at high masses, the systematic errors on the  $q_T$  plot are 6.4% at low  $q_T$  and 2.5% at high  $q_T$ , and the systematic errors on the  $\Delta\phi_{\gamma\gamma}$  plot are 360% at small opening angles and 3.2% near  $\pi$  (i.e. back-to-back). The two continuous curves in the figures correspond to two different theoretical predictions. The solid line represents the RESBOS prediction, and the dotted line represents the DIPHOX with the addition of the gluon-gluon box contribution at LO and NLO. The bin widths change as statistics allow for better mapping of the cross-section. Figure 6.11 shows a fall off in the cross-section at low masses. This is due to the transverse momentum cut on each photon. Above an invariant mass of about  $50 \text{ GeV}/c^2$  it is seen that the cross-section falls smoothly as a function of mass as predicted by both theoretical curves. Figure 6.12 also shows the cross-section falling with increasing  $q_T$  in general agreement with the theories, but it is noted that the DIPHOX prediction is significantly higher than the data at low  $q_T$ . Figure 6.13 also shows essential agreement between the data and the two theoretical predictions, indicating that most diphoton states are produced back-to-

### Ave Diphoton Mass Cross-Section

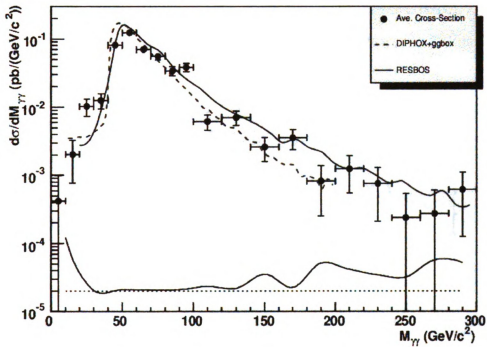


Figure 6.11. Differential diphoton cross-section as a function of mass.

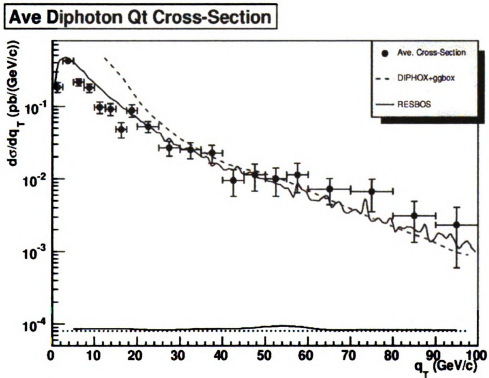


Figure 6.12. Differential diphoton cross-section as a function of  $q_T$ .

### Ave Diphoton Phi Cross-Section

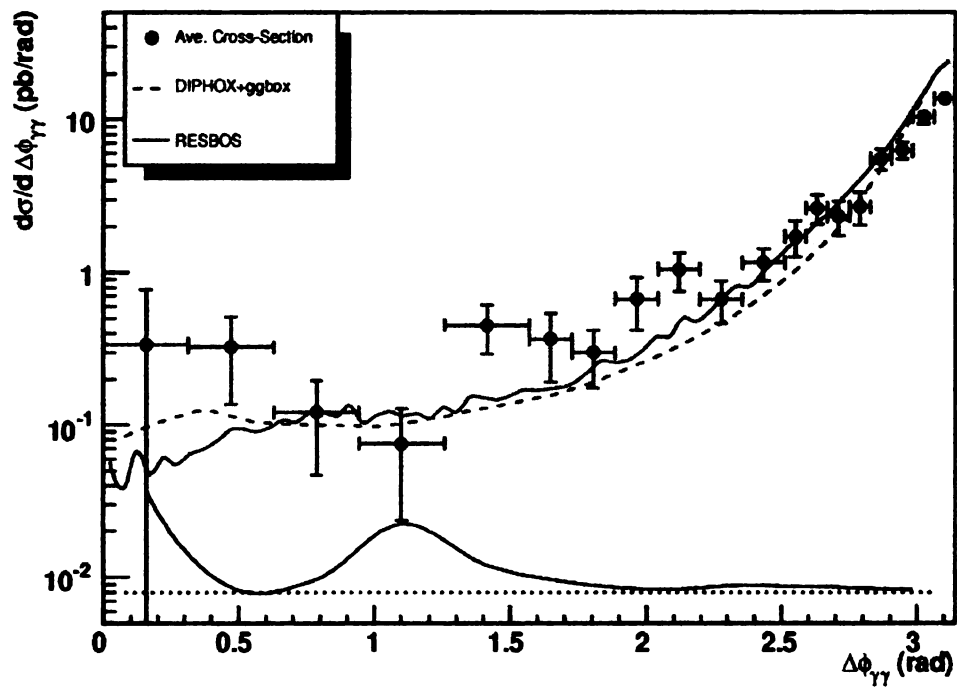


Figure 6.13. Differential diphoton cross-section as a function of opening angle.

back ( $\Delta\phi_{\gamma\gamma} \sim \pi$ ). When  $\Delta\phi_{\gamma\gamma}$  is far from  $\pi$ , the cross-section arises from the extra jet produced in the NLO calculations and is very sensitive to the isolation cuts made in this analysis. The theory predictions are also not well modeled in this region due to uncertainty in fragmentation function parameters.

# CHAPTER 7

## Conclusions

The differential cross-section of the direct diphoton process as a function of mass,  $q_T$ , and opening angle at  $\sqrt{s} = 1.96$  TeV has been measured using  $1046.19 \text{ pb}^{-1}$  of luminosity collected with the D0 detector between October 2002 and February 2006. The results shown are in good agreement with theory.

This measurement of the diphoton production at the Tevatron can be used to predict the QCD production at the upcoming LHC at CERN, which is scheduled to start within the next couple of years. This in turn will be useful in predicting the irreducible background to Higgs searches at LHC.

CDF has previously attempted this analysis in Run II with one-fifth of the data [42]. They are currently updating their analysis to include more statistics.

An alternative approach to the matrix inversion technique used here would be to cut on any or all of the three discrimination variables. This would increase the purity of the final sample which could then be used to study other aspects of the diphoton production (e.g. associated particle production). This method, however, would involve much larger inefficiencies and an unknown background contamination. It would also likely suffer from low statistics.

The cross-sections presented in Figures 6.11, 6.12, and 6.13 are the average of the cross-sections resulting from the application of each of the discrimination variables in

the matrix inversion technique. This averaging is likely not to be strictly accurate, especially if the three variables are coupled (as the CPS\_RMS and CPS\_RMSSQ variables are likely to be). Future analyses could study the interdependence of these variables and shed further light on the dynamics of diphoton production.

Further interesting analysis could be performed to study the non-perturbative QCD aspects of this process by implementing a  $q_T < M_{\gamma\gamma}$  cut. This cut should remove events containing perturbative effects such as the Feynman diagrams presented in Figure 2.3. The result of such a cut would be most pronounced in the opening angle plots by continuing to slope downward at 1.5 radians instead of leveling off. The differential cross-sections could also be measured as a function of other kinematic variables.

## BIBLIOGRAPHY

- [1] D. Griffiths, *Introduction to Elementary Particles.*, New York: John Wiley & Sons, Inc.; 1987.
- [2] L. Alvarez-Guamè, et al., “Review of Particle Physics.”, *Physics Letters B* 592: 31-78, 2004.
- [3] S.T. Thornton, A. Rex, *Modern Physics.*, Orlando, Florida: Saunders College Publishing; 2000.
- [4] T. Morii, C.S. Lim, and S.N. Mukherjee, *The Physics of the Standard Model and Beyond.*, River Edge, New Jersey: World Scientific Publishing Co., 2004.
- [5] A. Belyaev, A. Blum, R.S. Chivukula, and E.H. Simmons, “The Meaning of Higgs:  $\tau^+\tau^-$  and  $\gamma\gamma$  at the Tevatron and the LHC”, hep-ph/0506086, 2005.
- [6] C. Balázs, E. Berger, P. Nadolsky, C.-P. Yuan, “Calculation of Prompt Diphoton Production Cross-sections at Tevatron and LHC Energies”, arXiv:0704.0001, 2007.
- [7] <http://www.fnal.gov/pub/about/whatis/history.html> - accessed 7/20/2006
- [8] <http://nobelprize.org/physics/laureates/1938/fermi-bio.html> - accessed 7/20/2006
- [9] <http://www.fnal.gov/pub/inquiring/physics/accelerators/chainaccel.html> - accessed 7/20/2006
- [10] <http://www-bd.fnal.gov/public/chain.html> - accessed 7/20/2006
- [11] V.M. Abazov, et al., (D0 Collaboration), The Upgraded D0 Detector, *Nucl. Instr. and Methods A* {565}, 463 (2006).
- [12] S. Abachi, et al., (D0 Collaboration), The D0 Detector, *Nucl. Instr. and Methods A* 338 185 (1994).

- [13] F. Halzen and A. Martin, *Quarks & Leptons.*, New York: John Wiley & Sons, Inc.; 1984.
- [14] Perkins, Donald H., *Introduction to High Energy Physics.*, Reading, Massachusetts: Addison-Wesley; 1972.
- [15] D.Adams, et al., The D0 Upgrade: Central Fiber Tracker, Technical Design Report, D0 Note 4164.
- [16] J. Bartels, et al., The European Physical Journal C, Volume 15, Number 1-4, 2000, pg. 80.
- [17] Alexander Melnitchouk, Ph.D. Thesis, Brown University, Providence, RI, 2004 (unpublished).
- [18] T. LeCompte, T. H. Diehl, The CDF and D0 Upgrades for Run II, Annu. Rev. Nucl. Part. Sci. 2000. 50:71-117.
- [19] <http://www-d0.fnal.gov/Run2Physics/cs/caf/docs/Tutorial-Vancouver.pdf> - accessed 7/20/2006.
- [20] [http://www-d0.fnal.gov/trigger\\_meister/private/www/tl\\_desc/global.html](http://www-d0.fnal.gov/trigger_meister/private/www/tl_desc/global.html).
- [21] J. Hays, V. Kaushik, J. Mitrevski, O. Mundal, C. Schwanenberger, “Electron Trigger Efficiencies using Calorimeter Information in p17 Data”, D0 Note 5138.
- [22] A. Ferapontov, Y. Maravin, “Study of  $Z(\gamma) \rightarrow ll\gamma$  events in D0 Run II p17 Data”, D0 Note 5156.
- [23] D. Bandurin, G. Golovanov, D. Korablev, N. Skachkov, “Measurement of Triple Differential Photon Plus Jet Cross Sections in  $p\bar{p}$  Collisions At 1.96 TeV In D0”, D0 Note 5369.
- [24] J. Hays, J. Mitrevsi, C. Schwanenberger, T. Toole, “Single Electron Efficiencies in p17 Data and Monte-Carlo Using d0correct from Release p18.05.00”, D0 Note 5105.
- [25] [http://www-d0.fnal.gov/d0dist/dist/packages/photon\\_id\\_tools/](http://www-d0.fnal.gov/d0dist/dist/packages/photon_id_tools/).
- [26] <http://root.cern.ch/>.
- [27] Torbjörn Sjöstrand, Leif Lönnblad, Stephen Mrenna, Peter Skands, *PYTHIA 6.3 Physics and Manual*, hep-ph/0308153, 2003.

- [28] W.K. Tung, et al., “Heavy quark mass effects in deep inelastic scattering and global QCD analysis”, hep-ph/0611254, 2007.
- [29] R. Brun and F. Carminati, CERN Program Library Long Writeup W5013, 1993
- [30] C. Balázs and C.P. Yuan, “Soft Gluon Effects on Lepton Pairs at Hadron Colliders”, hep-ph/9704258, 1997.
- [31] T. Binoth, E. Pilon, J.Ph. Guillet and M. Werlen, Eur. Phys. J., C 16, 311, 2000.
- [32] C. Balázs, E. Berger, P. Nadolsky, C.-P. Yuan, “All-orders Resummation for Diphoton Production at Hadron Colliders”, hep-ph/0603037, 2006.
- [33] J.Ph. Guillet, Private Communication.
- [34] C. Schmidt, Private Communication. See also Z. Bern, L. J. Dixon, and C. Schmidt, Nucl. Phys. Proc. Suppl. **116**, 178 (2003). [arXiv:hep-ph/0211206].
- [35] J. Bartels, et al., The European Physical Journal C, Volume 15, Number 1-4, 2000, pg. 27.
- [36] [http://www-d0.fnal.gov/phys\\_id/emid/d0\\_private/certification/main\\_v5\\_0.html](http://www-d0.fnal.gov/phys_id/emid/d0_private/certification/main_v5_0.html) - accessed 05/13/07
- [37] G. Bernardi, B. Olivier, B. Knuteson, M.Strovink, “NADA: A New Event by Event Hot Cell Killer”, D0 Note 3687.
- [38] R. Zitoun, “Study of the Non Linearity of the D0 Calorimeter Readout Chain”, D0 Note 3997.
- [39] A. Harel, “Jet ID Optimization”, D0 Note 4919.
- [40] O. Atramentov, et al., “Photon Identification in p17 Data”, D0 Note 4976.
- [41] A. Askew, D. Duggan, “CPS Variables for Photon Identification”, D0 Note 4949.
- [42] D. Acosta, et al., “Measurement of the Cross Section for Prompt Diphoton Production in  $p\bar{p}$  Collisions at  $\sqrt{s} = 1.96$  TeV”, arXiv:hep-ex/0412050, 2005.

MICHIGAN STATE UNIVERSITY LIBRARIES



3 1293 02956 0681